Mathematical modeling of local perfusion in large distensible microvascular networks

Paola Causin[a], Francesca Malgaroli

[a]*Dept. of Mathematics, Università degli Studi di Milano, Italy*
e-mail: paola.causin@unimi.it

Abstract

Microvessels -blood vessels with diameter less than 200 μm- form large intricate networks, functionally organized into arterioles, capillaries and venules. In these networks, the distribution of flow and pressure drop stems in a complex manner from single vessel behavior and mutual vessel interactions. In this paper we propose a mathematical and computational model to study the behavior of large networks of compliant microvessels. The network geometry is simplified for computational purposes. The arteriolar and venular trees are represented by graphs of straight cylinders, each one corresponding to a vessel. The two trees are connected through a capillary bed. The blood flow and pressure drop across each vessel are related via a simplified fluid-structure interaction (FSI) model, represented by a generalized Ohm's law featuring a conductivity parameter. The conductivity is a function of the vessel cross section area (shape and area), which, in turn, undergoes deformations due to luminal and external pressure loads. The membrane theory is used for the description of the deformation of vessel lumina, adapted to consider thick–walled arterioles and thin–walled venules. An original point of the present work is represented by the inclusion of a buckling model in the FSI problem for venules. As a matter of fact, venules can experience negative values of transmural pressure (difference between luminal and interstitial pressure) and may assume a deformed and even collapsed configuration due to their minimal cross-sectional bending stiffness. The complete model including flow in distensible arterioles, capillaries and venules represents a nonlinear coupled system of PDEs, which is approached numerically by finite element discretization and linearization techniques. As an example of application, we use the model to simulate flow in the microcirculation of the human eye retina, a terminal system with a single inlet and outlet. After a

phase of validation against experimental measurements of the correctness of the blood flow and pressure fields in the network, we compute the network response to different conditions. Significant redistributions of the blood flow in the network are observed, highlighting the importance of considering the single vessel behavior along with its position and connectivity in the network.

Keywords: Regional Blood Flow; Vessel Buckling; Vascular Resistance; Retinal Microcirculation; Distensible Blood Network; Mathematical Model

1. Introduction

Microscopic blood vessels play the vital role of locally perfusing single body's organs. Microcirculatory plexi include thousands of microvessels (diameter less than 200 μm), functionally categorized into arterioles, capillaries or venules. First elementary assessments of microcirculatory mechanisms on skin or superficial organs date back at least to the 18^{th} century [1]. At present, techniques like positron emission tomography, magnetic resonance imaging and contrast echography allow to study in a non–invasive manner regional blood flow in internal organs of human patients. The information content of such measurements is, however, far to be complete. Data as network geometry, fluid-dynamics pressure and flow fields -in physiological conditions or in altered conditions/provocation studies- can be rarely collected in a coherent and comprehensive manner in multiple locations of the network. Resolution limitations in smaller vessels and uncertainty in physical parameters add further difficulties [2, 3]. Altogether, these issues strongly motivate the use of theoretical and computational models to reduce the present gap in knowledge.

Mathematical models in hemodynamics are consistently present in literature since the early 1960s. A significant part of these models address the simulation of a limited number of vessels of major size like the aorta and collaterals, possibly coupled with reduced–order models for the rest of the circulatory system (see, *e.g.*, the review works [4, 5] and the very recent [6]). The modeling of microvessels has on its own a long history, dating back to the pioneering work of Krogh at the beginning of the 20th century (see, *e.g.* [7]). Several important features characterize the microcirculation: *a)* microcirculatory networks include a huge number ($> 10^4$) of interconnected vessels with complex behavior, so that the computational cost can quickly

exceed available resources; *b)* the flow in microvessels is essentially of resistive type [3]. The flow is essentially determined by the balance of viscous stress and pressure gradient. The Reynolds and the Womersley numbers are smaller (or much smaller) than 1, making -at least in a first approximation- inertia and pulsatility negligible; *c)* the regulation of blood flow through a microcirculatory network is determined by both passive and active forces. Blood flow creates a pressure inside the vessel lumen that distends the vessel and contrasts the pressure exerted from the outside by interstitial fluids, organs, and cytoskeletal structures. The difference between the internal and external pressure, known as transmural pressure, is balanced by the circumferential tension generated within the vessel wall. Such a tension includes two main components, a passive tension and active tension. The passive tension - common also to larger vessels - is generated by the structural components of the vessel wall such as collagen and elastin fibrils. The active tension is instead peculiar to microcirculation and arises in arterioles due to the contraction of their thick muscular walls under the influence of vasoactive agents (oxygen, carbon-dioxide, nitric oxide, just to cite a few).

Several models of microcirculation use compartmental representations as the milestones works by Ursino and co-authors (see *e.g.*, [8, 9]) or use sets of representative segments corresponding to vessels of different size (for example regrouping large/small arterioles and venules, see, *e.g.*, [10, 9, 11]). These approaches allow to maintain a low number of unknowns and have been used to investigate many aspects. For example, with a similar technique Fantini has analyzed in [12] the role of the microcirculatory network nested in the whole brain circulation system was investigated. What is lost with these approaches is the spatial distribution of field variables. Relevant geometrical and physical heterogeneities of the network cannot be represented, as well as complex internal interactions (see [13] for a discussion on this topic). Spatial heterogeneity is taken into account in a different category of works, which consider the network topology and use anatomically coherent geometrical data. Vessel trees can be constructed *ex-novo* by means of mathematical algorithms and relevant morphological and topological information is used to obtain realistic physics. For example, the use of principles of fractal geometry to define the diameter of daughter vessels sprouting from a bifurcation and build a with a controlled degree of asymmetry has been proposed by Takahashi in [14] and used by the authors of the present work in [15]. The network geometry (vessel radii and lengths) can also be extracted from digitized images of ex-

perimental measures (see the relevant works [16, 17]). While these models include the effect of the geometrical localization of each vessel in the network, the mechanical description is completely absent (the vessels are rigid-walled pipes) or very limited. In this latter case, phenomenological vessel compliance laws are often used. These laws reproduce selected structural behaviors in a simplified setting derived from semi-empirical relations. Furthermore, none of these models considers the fact that microcirculatory networks can experience severe reductions of the luminal cross section, till collapse. As a matter of fact, these networks are characterized by low values of the luminal pressure that are comparable to the surrounding interstitial pressure, both in physiological conditions and -more dramatically- in presence of pathologies. The very few works addressing the buckling phenomenon locate themselves at two opposites. Some of these studies consider a single vessel (or very small networks) using complex descriptions, possibly 3D and anatomically accurate [18, 19, 20, 21, 22, 23]. Alternatively, other studies model mid-sized/large microvascular networks including a Starling/collapsible components [24, 8, 9] or phenomenological variations of the physical parameters (see [25] in a slightly different context). While the first approach cannot be applied to large networks due to its huge computational cost, the second one is much more efficient but it does not consider the sophisticated coupling between vessel mechanics and pressure loads. These facts limit, from both the viewpoints, the spectrum of phenomena which can be analyzed.

In this article, we propose a mathematical model of general microcirculatory districts which is capable of dealing with large compliant networks with an affordable time of resolution. The work is inspired, but not exclusively, from the approaches used to study relatively small vessel graphs as a collection of 1D distensible tubes described by simplified, yet physically consistent, mechanical laws (see [26, 27, 28, 29, 30]). In the microvascular plexi object of our analysis, blood flow regulation is obtained by variation of the vessel diameter under the effect of both passive and active (with limitation to the arterioles provided of a thick muscular wall) actions. In this work, we focus our attention on the first set of mechanisms, investigating the role of geometrical and structural (the so-called "physical") factors in flow regulation. Describing active regulation mechanisms requires a model for blood–tissue solute exchange. These aspects are beyond the scopes of the present work.

The key point in our analysis is the effect of vessel compliance on vessel resistivity. Compliant microvessels deform under mechanical loads. The

shape of the luminal domain is thus altered. This implies a variation in the resistance to flow and, in turn, a redistribution of the flow itself in the network. To address this problem, we consider a simplified fluid–structure interaction approach. Blood flow in each vessel is modeled by a generalized Poiseuille's law, featuring a conductivity parameter dependent on the area and shape of the vessel cross section. A thick or thin–wall structural model of membrane - chosen according to the physiological vessel wall thickness-to-radius ratio [31, 32]- is used to compute the deformed cross section. In addition, our approach includes a buckling model for thin–walled vessels derived from [33]. Buckled vessels lose their original circular–shaped cross section and assume an elliptical or dumb–bell configuration. The result is a strong increase of vessel resistance to flow. The model can withstand partial or total vessel blockage, providing a quantitative study of the fluid-dynamic state of the network. Even if there is a clear connection of the present model with a Starling resistor description, more information is obtained. The present model can represent partial patency to flow and allows to reconstruct a topological information.

We apply the proposed model to the simulation of blood flow in the retinal circulation. To do this, we consider the network geometries proposed by Takahashi and colleagues [34, 14]. The resulting network is composed of more than 9000 vessels, with a tunable degree of asymmetry. After validating of the model against experimental measures (data from [35]), we carry out different sets of studies: *i)* we globally increase the external pressure, reaching the conditions for buckling to occur. We observe that the luminal pressure gradually increase along all the network, till buckling, after which a discontinuity in the behavior takes place, with a much more marked pressure increase and flow redistribution; *ii)* we examine the system behavior in a parametric study in which we monitor how the flow rate varies with the overall pressure drop applied between the upstream and downstream ends of the network; *iii)* we locally increase the external pressure inside a spherical region located in correspondence of a region of the post–capillary venules. Simulation results show how this perturbation extends its effect till four or five vessels generations away, with important redistribution of flow and resistance. An interesting, noticeable, key point emerging from the above results is the importance of vessel localization in the network. Vessels with the same mechanical and geometrical properties but laying in two different regions of the network display a pretty different behavior due to their local pressure levels and interaction with other vessels.

The paper is organized as follows: in Sect. 2 we present our mathematical model for microcirculatory districts. Namely, in Subsect. 2.2 we introduce the mathematical model for blood flow in a single vessel and the generalized Ohm's law connecting flow rate and pressure drop via the conductivity parameter. This latter is obtained in a coupled manner from the wall structure models as discussed in Subsect. 2.3 in pre–buckling conditions (see 2.3.1), where a particular attention is devoted to the Young modulus choice, and buckled conditions (see 2.3.2). In Sect. 2.4, we report a summary of the computation of the conductivity parameter. In Sect. 2.5, we discuss the importance of using a correct unloaded configuration, describing the numerical technique applied to compute it from measurements. In Sect. 3, we introduce the nomenclature to deal with a network and we present the conditions to couple single vessels converging in a node. In Sect. 4, we provide a summary of the model (see 4.1) and we discuss the numerical procedure employed to discretized the fully coupled problem (see 4.2). Then, in Sect. 5, we first introduce the network geometries we will use in simulations (see 5.1) along with the physical parameters (see 5.2) then, we present the results of the numerical simulations in different test cases (see 5.3). Eventually, in Sect. 6, we draw the conclusions, discussing the results along with their significance, the limitations of the model and the forthcoming work.

2. Microcirculation model

2.1. Geometrical model

The geometry, denoted in the following as the "measured geometry", of the network can be originally derived from digitized images or can be constructed *in silico* on a computer on the basis of anatomical data. In any case, our starting point is the 1D skeleton of the network along with its topological connectivity and cross sections and lengths distribution. Each segment of the skeleton represents a blood vessel and can branch at nodal junctions. To increase the computational accuracy, we introduce further subdivisions into elements on each segment (see [20] for a similar approach). We establish on each element a local system of cylindrical coordinates and we let the z-axis coincide with the element axis, arbitrarily choosing its orientation. The vessel element is endowed of the 3D structure of a straight cylinder of axis z, with uniform, but not necessarily circular, cross section. The r and θ coordinates lay in the plane of the vessel cross section (see Fig. 1). Elements belonging to the same vessel share homogeneous mechanical properties. From

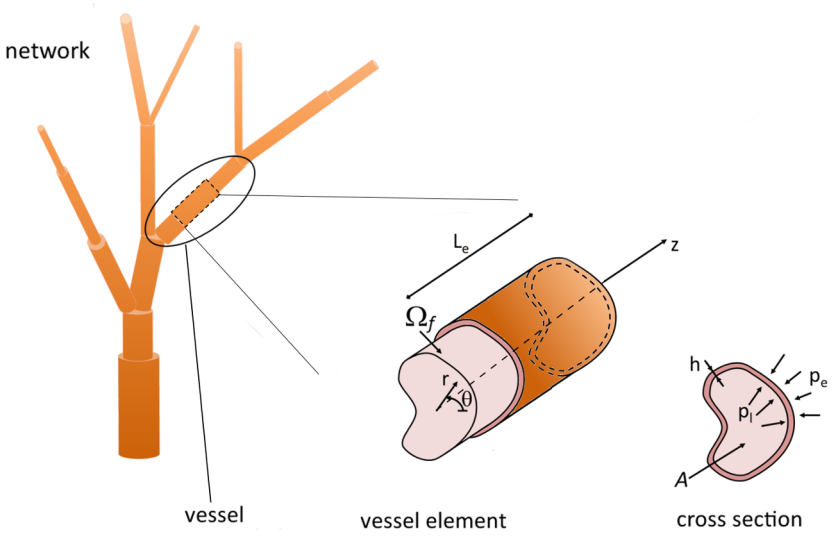

Figure 1: Schematic representation of a portion of a microcirculatory network. Each vessel is described as a duct with straight longitudinal axis and is further partitioned into a series of consecutive short elements of arbitrary but constant cross section shape along the axis. The central part of the figure depicts one of such elements, of constant length L_e, with highlighted the domain Ω_f occupied by the blood flowing inside the luminal space and the wall structure. The right part of the figure represents the cross section A of the luminal space along with the thickness h of the vessel wall. The wall is internally loaded with pressure p_{l} from fluid actions and externally loaded with given interstitial pressure p_{e}. The local system of coordinates (r, θ, z) on the element is represented as well.

this geometrical model, we proceed by computing a reference ("unloaded") configuration as described in Sect. 2.5. This latter geometry represents the mathematical domain of the present model.

2.2. Blood flow model

The domain occupied by blood inside the vessel element (luminal space) is defined as (see Fig. 1)

$$\Omega_f = A \times (0, L_e)$$

where $A = (0, R(\theta)) \times (0, 2\pi)$, $R(\theta)$ being the position of the blood–wall interface and where L_e is the element length.
The following assumptions are introduced:

1. blood is modeled as a Newtonian incompressible fluid with dynamic viscosity μ;
2. the "radial" scale of motion is much smaller than the "longitudinal" one, so that only a longitudinal velocity is considered;
3. convective terms and pulsatility are negligible, since in this region the Reynolds and the Womersley numbers are smaller (or much smaller) than 1. Inertia forces are less important and the flow is essentially determined by the balance of viscous stress and pressure gradient (resistive flow, [3]).

Letting p be the fluid pressure and u the axial velocity, the continuity and momentum balance equations read:
find p and u such that

$$\frac{\partial u}{\partial z} = 0, \qquad \Delta_{r\theta} u = \frac{1}{\mu}\frac{\partial p}{\partial z}, \qquad \frac{\partial p}{\partial r} = \frac{\partial p}{\partial \theta} = 0 \qquad \text{in } \Omega_f, \tag{1}$$

where $\Delta_{r\theta}(\cdot)$ is the Laplace operator with respect to the (r, θ) coordinates. No-slip conditions are considered on $\partial A \times (0, L_e)$. Notice that the pressure field resulting from Eqs. (1) has a constant gradient in the axial direction. Moreover, the pressure is uniform on each section, so that, straightforwardly, the fluid pressure p_{l} acting on the internal surface of the wall structure is equal to p.

We now proceed to obtain a form of Eqs. (1) which is amenable to be efficiently coupled with wall structure equations in the context of a large network of vessels. Introducing the non–dimensional variables $r^* = r/\widehat{R}$ and $u^* = (-\mu \left(\widehat{R}^2 dp/dz\right)^{-1})u$, $\widehat{R}$ being a characteristic linear dimension of the cross section, we write the dimensionless form of Eq. $(1)_2$ as [36]:
find u^* such that

$$-\Delta_{r^*\theta}\, u^* = 1 \qquad \text{in } A^*, \tag{2}$$

where $A^* = A/\widehat{R}^2$, and $u^* = 0$ on ∂A^*. We use the solution u^* of (2) to define the conductivity parameter [33]

$$\sigma = \frac{\widehat{R}^4}{\mu} \int_{A^*} u^* dA^*, \tag{3}$$

so that the expression of the volumetric flux of fluid

$$Q = \int_A u\, dA = -\frac{1}{\mu}\frac{dp}{dz}\, \widehat{R}^4 \int_{A^*} u^* dA^* \tag{4}$$

can be re–formulated as the generalized Ohm's law connecting flux and pressure gradient

$$Q = -\sigma \frac{dp}{dz}. \tag{5}$$

Notice that the conductivity σ is a function of the geometry of the vessel cross section, this latter being itself an unknown of the problem. The coupling with a structural model for the vessel wall through the pressure loads closes the problem.

We now go back to the original fluid balance equations (1) and we integrate Eq. $(1)_1$ on the cross section area. Gathering the resulting equation and the Ohm's law (5), we obtain the (equivalent) system: find Q and p such that

$$\frac{dQ}{dz} = 0, \qquad Q = -\sigma \frac{dp}{dz} \qquad \text{in } \Omega_f. \tag{6}$$

Remark 1. *Observe that the fluid-structure interaction coupling makes system* (6) *nonlinear, since, as stated by Eq.* (3)*, the conductivity is a function of the vessel cross section geometry by itself and also through the expression of the dynamic viscosity. As a matter of fact, this latter depends, among the others, on the vessel cross section diameter (more generally speaking on the hydraulic diameter), as detailed in Sect. 5.2.*

Remark 2. *From system* (6)*, it appears that the conductivity parameter must be constant in each vessel element, due to the linearity of the pressure and the constancy of the flux in the axial direction. For this reason, we couple the fluid with the structure by considering this latter to be loaded on the lumen interface with a uniform pressure $\overline{p}$, function of p (for example, its average along the element length). This choice results in having $\sigma = \sigma(\overline{p})$. We notice that this approximation is acceptable if the pressure jump at the element is not excessively high.*

2.3. Vessel wall model

In order to compute the vessel conductivity from Eq. (3), we need to dispose of the vessel cross section area and shape as a function of the pressure loads. In other words, we must build via a structural model a tube law, mathematically connecting the vessel cross section area with the transmural pressure p_{t}, defined as the difference between the luminal pressure p and the interstitial pressure p_{e} [37]. We anticipate in Fig. 2 the tube law resulting

from the present model. Observe, in particular, the different behavior of arterioles (thick-walled vessels) and venules (thin–walled vessels). Observe also how, for these latter, there exists a physiologically plausible value of transmural pressure under which the tube is not any more circular but assumes a buckled configuration. Notice that the cross section does not need to be completely closed for the vessel to be "functionally lost to the network". As a matter of fact, it suffices the section to be small enough to prevent red blood cells passage to compromise its physiological function [29].

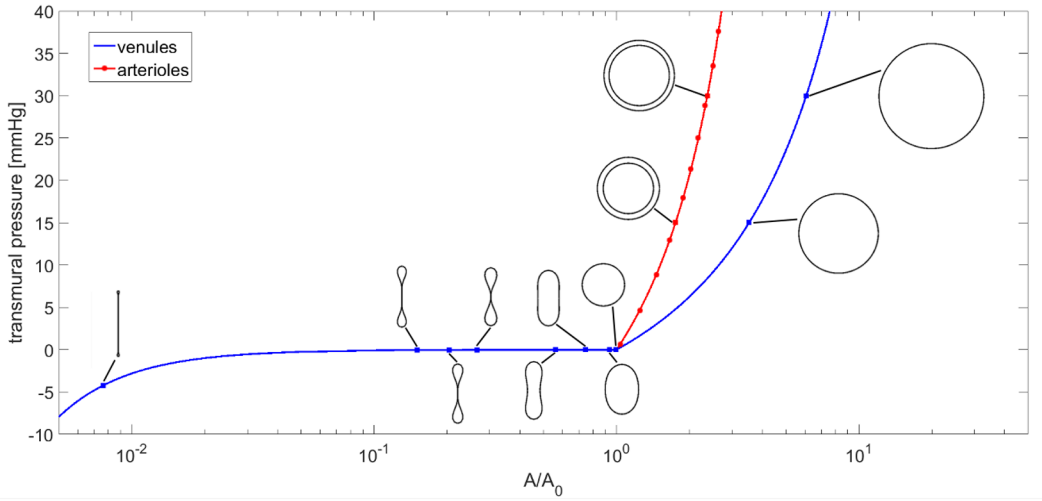

Figure 2: Tube laws (transmural pressure vs. area relations) for arterioles and venules as obtained from the present model. As customary when representing this curve, the cross section area is normalized over the cross section area at zero transmural pressure. Characteristic cross sections are sketched for various values of the transmural pressure. Observe in proximity of zero transmural pressure the presence of a "snap action" in venules, *i.e.*, a change in shape over a pressure range so small as to be considered negligible. Venules with $A/A_0 < 10^{-2}$ are practically collapsed. The curves are obtained using the same data considered for Fig. 8.

In the structural model, each vessel element is modeled as an elastic ring made of elastic (Young modulus E) and incompressible material (ν=0.5), assumed to be circular in undeformed conditions (radius R_u, thickness h_u). The same cylindrical coordinate system of the fluid model is considered, if not otherwise specified. Small deformations are considered, similarly to several works in this field, see *e.g.*, [38, 4]. In Fig. 3, we report the notation required for the mathematical discussion and the definition of the relevant configurations we will consider.

2.3.1. Structural model for pre–buckling transmural pressure

On applying the internal and external pressure loads, radial and circumferential stresses arise in the ring. We assume axi-symmetry and plane stress conditions. Let $\eta = \eta(r)$ be the radial displacement of a point of the vessel wall. Then, we establish the strain–displacement relations (refer also to Fig. 4)

$$\varepsilon_N = \frac{d\eta}{dr}, \qquad \varepsilon_T = \frac{\eta}{r}, \tag{7}$$

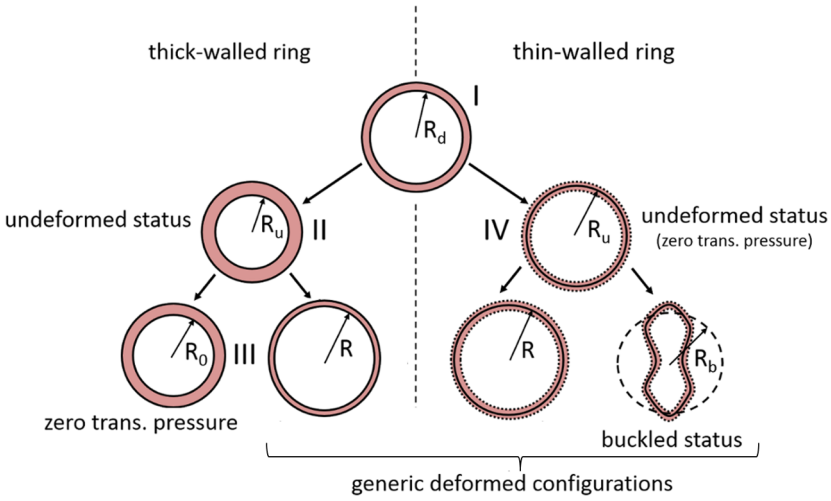

Figure 3: Characteristic configurations in the structural models. Configuration I is the experimentally measured "*in-vivo*" geometry, supposed to be circular. The arrows indicate the steps followed in the computations to obtain a certain configuration from this configuration. According to the different modeling chosen as a function of the wall thickness-to-radius ratios (see Sect. 2.3.1), the left side of the figure refers to thick–walled rings (the internal radius is indicated), while the right side to thin–walled rings (the mean fiber radius is indicated). Configurations II and IV are the unloaded configurations, corresponding to the stress-free geometry for the thick–walled ring and to the zero transmural pressure geometry in the thin–walled ring, respectively. Notice that in the case of a thick–walled ring the undeformed geometry II differs from the zero transmural pressure geometry III. We refer to Sect. 2.5 for a detailed discussion on the computation of the unloaded configuration. In the last row, we represent generic deformed geometries of the thick and thin–walled ring cross sections, respectively. In the case of the thin–walled ring, we also consider the possibility of section buckling, so that the generic deformed cross section is circular if in pre–buckling conditions (left) or with a non–circular shape if in buckled conditions (right). The same terminology adopted for the radii also applies to the vessel wall thicknesses in the various conditions.

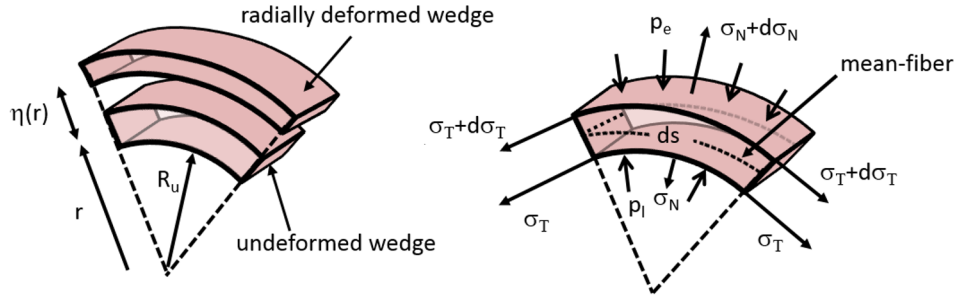

Figure 4: Infinitesimal wedge–shaped radial section used for the derivation of the balance equations for ring model with circular cross section. Left: radial deformation. Right: tangential (hoop) stress σ_T, normal (radial) stress σ_N with their increments acting on the wedge faces, along with the pressure loads.

ε_N being the radial strain and ε_T the circumferential strain, respectively, and the elastic constitutive equations

$$\sigma_N = \frac{E}{1-\nu^2}(\varepsilon_N + \nu\varepsilon_T), \qquad \sigma_T = \frac{E}{1-\nu^2}(\varepsilon_T + \nu\varepsilon_N), \tag{8}$$

σ_N being the principal radial stress and σ_T the principal hoop stress, respectively, and $E = E(p_\mathrm{t})$ a functional representation of the Young modulus (see Appendix B for a complete discussion on this topic). We close the problem considering the equilibrium equation

$$\frac{d\sigma_N}{dr} + \frac{1}{r}(\sigma_N - \sigma_T) = 0, \tag{9}$$

with boundary conditions $\sigma_N(R_u) = -p$ and $\sigma_N(R_{u,e}) = -p_e$, with $R_{u,e} = R_u + h_u$. Eq. (9) combined with (8) and (7) and the relative boundary conditions gives

$$\sigma_N = B_1 + \frac{B_2}{r^2}, \qquad \sigma_T = B_1 - \frac{B_2}{r^2}, \tag{10}$$

with $B_1 = \dfrac{pR_u^2 - p_\mathrm{e}R_{u,e}^2}{R_{u,e}^2 - R_u^2}$ and $B_2 = \dfrac{R_u^2 R_{u,e}^2(p_\mathrm{e} - p)}{R_{u,e}^2 - R_u^2}$.

A useful simplification of the expressions in Eq. (10) can be obtained for thin–walled structures, since in this case $h_u, h_u^2 \ll R_{m,u}$, with $R_{m,u} = (R_u + R_{u,e})/2$ (virtual position corresponding to the mean fiber radius). We

then obtain the approximations

$$\sigma_N \simeq 0, \qquad \sigma_T \simeq p_t \frac{R_{m,u}}{h_u}, \tag{11}$$

where the second relation represents the well–known Laplace's law. Thin–wall models are considered admissible till $\gamma \simeq 1{:}10$ [37], γ being the ratio between the thickness of ring with respect to the radius. As shown in Fig. 5, the venule wall can thus be considered a thin structure, since γ is in the range 1:20 to 1:50. Much different is the situation for arterioles, for which $\gamma \simeq 1:3$, and thus the use of the full expressions in Eq. (10) is required.

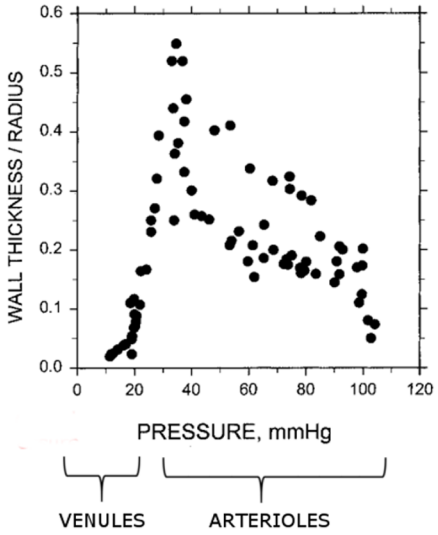

Figure 5: Wall thickness relative to inner vessel radius (parameter γ in the model) as a function of intravascular pressure (image adapted from [39], data obtained from a meta–analysis of literature studies). Arterioles and venules are designed to withstand different ranges of luminal pressure. The arteriolar wall is thus a thick membrane structure, while the venular wall is a thin membrane structure. Further, similar, data can be found in [40, 41].

In order to derive the expression of the cross section deformed radius, we combine Eqs. (8) with (7) and Eq. (10) (for thick rings) or Eqs. (11) (for thin

rings), respectively, obtaining

$$\begin{cases} R = R_u \left(1 + \dfrac{(1-\nu)}{E} B_1 - \dfrac{(1+\nu)}{E} \dfrac{B_2}{R_u^2}\right) & \text{thick–walled ring,} \\ R = R_u \left(1 + \dfrac{(1-\nu^2)}{\gamma E} p_{\mathrm{t}}\right) & \text{thin–walled ring,} \end{cases} \tag{12}$$

where for thick vessels R denoted the internal radius (blood–vessel interface) while, with a slight abuse of notation, for thin vessels R denotes the mean fiber radius. The deformed ring thickness can be post-computed from incompressibility, yielding $h = \sqrt{R^2 + h_u^2 + 2h_u R_u} - R$ for thick vessels and $h = h_u R_u / R$ for thin vessels.

2.3.2. Structural model for buckled thin–walled rings

When considering the possibility of reaching buckled configurations, the model must also keep into account the bending actions which actually lead to the loss of axi-symmetry. It is convenient in this context to fix a system of Cartesian axes on the bottom point of the section (see Fig. 6, left). We let s be the arc–length parameter describing the wall mid-line in counterclockwise direction from the origin of the axes and we denote by $\varphi = \varphi(s)$ the angle between the positive direction of the x axis and the tangent to the cross section. The Cartesian coordinates $x = x(s), y = y(s)$ of a point P identified by arc-length s are given by

$$x = \int_0^s \cos(\varphi)\, ds, \quad y = \int_0^s \sin(\varphi)\, ds. \tag{13}$$

Fig. 6(right) shows an element wedge of arch length ds along with the normal stress σ_N, the tangential stress σ_T and the bending moment M arising from the pressure loads. According to the hypothesis of thin–walled structure, internal actions have a constant average value in the radial direction. Let $\mathcal{K}(s) = \dfrac{d\varphi}{ds}$ be the local curvature of the section and $\widehat{\mathcal{K}} = 1/R_u$ the curvature of the circular undeformed geometry taken as reference configuration. From the approximate theory of curved beams (see, *e.g.*, [42]), the bending moment $M = M(s)$ has the constitutive form

$$M = EI \left(\mathcal{K} - \widehat{\mathcal{K}}\right), \tag{14}$$

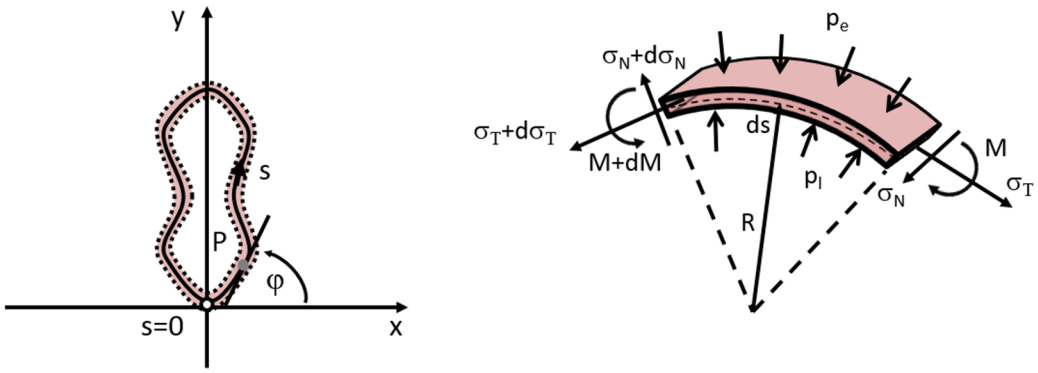

Figure 6: Left: coordinate system for the thin–walled ring model in buckled configuration. Right: tangential (hoop) stress σ_T, normal (radial) stress σ_N and bending moment M with their increments acting on the wedge faces, along with the pressure loads.

where EI is the flexural rigidity, E being the Young modulus (assumed here to be constant and equal to the basal value one for total lack of data) and $I = h_u^3/12$ the area moment of inertia of the cross section per unit length. The balance of bending moments and forces on the infinitesimal wedge–shaped radial section of ring per unit axial length is given by

$$\frac{dM}{ds} = \sigma_N h, \qquad \frac{d\sigma_N}{ds} = \mathcal{K}\sigma_T - \frac{p_\mathrm{t}}{h}, \qquad \frac{d\sigma_T}{ds} = -\mathcal{K}\sigma_N. \tag{15}$$

Combining Eqs. (15) with the Eq. (14) and using the definition of the curvature, yields the nonlinear boundary value system

$$\frac{d}{ds}\begin{pmatrix} \varphi \\ \mathcal{K} \\ \sigma_N \\ \sigma_T \end{pmatrix} = \begin{pmatrix} \mathcal{K} \\ \dfrac{\sigma_N h}{EI} \\ \mathcal{K}\sigma_T - \dfrac{p_\mathrm{t}}{h} \\ -\mathcal{K}\sigma_N \end{pmatrix}. \tag{16}$$

Linear stability analysis of system (16) (see, *e.g.*, [43]) shows that a buckled non–axisymmetric solution exists for every pressure $p_\mathrm{t} < p_\mathrm{t,b}$, where $p_\mathrm{t,b} = -3EI/R_b^3$ is the critical transmural pressure corresponding to the lowest energy mode (azimuthal wavenumber equal to 2). When $p_\mathrm{t} = p_\mathrm{t,b}$, the cross section (of radius R_b in incipient buckling) loses its circular shape due to physical instability and buckles into an elliptical shape.

For $p_{\rm t} < p_{\rm t,b}$, progressively, the nearest opposite sides of the section get close, until they touch if the contact pressure $p_{\rm t,c}$ is reached. The contact point becomes a straight line segment in contact if the pressure lowers to the contact line pressure $p_{\rm t,cl}$. As the pressure is further decreased, the length of the contact line increases and the associated section area tends to zero forming a dumbbell–like shape (see the characteristic shapes reported in Fig. 2).

The buckled configurations have a two-fold symmetry (since they are related to the wavenumber 2), which allows for solving system (16) just in a fourth of the domain. The approach to solve system (16) depends on the value of the transmural pressure, and namely:

i) for $p_{\rm t,cl} < p_{\rm t} < p_{\rm t,b}$, we compute numerically the solution under the hypothesis of isoperimetrical transformations (see also [44] for a similar assumption) using the boundary conditions given in [33]. We refer to Appendix A for more details of this computation;

ii) for $p_{\rm t} < p_{\rm t,cl}$, the solution of (16) can be found from that for $p_{\rm t} = p_{\rm t,cl}$ by the similarity transformation [33]

$$\begin{aligned} &\varphi(s) = \varphi_{\rm cl}(s_{\rm cl}), \quad \mathcal{K}(s) = (p_{\rm t}/p_{\rm t,cl})^{1/3}\mathcal{K}_{\rm cl}(s_{\rm cl}), \\ &\sigma_N(s) = (p_{\rm t}/p_{\rm t,cl})^{2/3}\sigma_{N,{\rm cl}}(s_{\rm cl}), \quad \sigma_T(s) = (p_{\rm t}/p_{\rm t,cl})^{2/3}\sigma_{T,{\rm cl}}(s_{\rm cl}), \end{aligned} \tag{17}$$

with the coordinate transformation $s = (p_{\rm t,cl}/p_{\rm t})^{1/3}s_{\rm cl}$, where $0 < s_{\rm cl} < s_1$, s_1 being the arc–length of the point of contact in the configuration corresponding to $p_{\rm t} = p_{\rm t,cl}$.

Once the solution of system (16) has been computed, the non–circular buckled geometry of the section is reconstructed in Cartesian coordinates from Eqs. (13).

The following case study shows an application of the above described model and the hemodynamic consequences of vessel buckling. We consider a single thin–walled vessel (venule) with inlet pressure $p_{\rm in} = 40$ mmHg and $p_{\rm e} = 18$ mmHg and we study the flux for outlet pressure $p_{\rm out}$ decreasing monotonically in the range $[20, 10]$ mmHg. The vessel has undeformed radius equal to 30 μm and length equal to 370 μm. Simulations are run dividing the vessel into $N_e = 800$ consecutive elements, with progressively smaller elements as the end of the tube is approached. In Fig. 7(left), we show the flux as a function of the outlet pressure. When this latter is decreased, blood flow

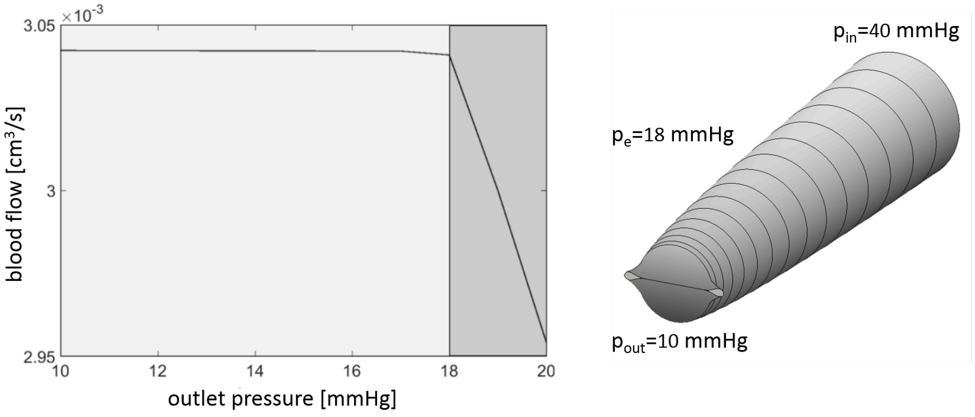

Figure 7: Buckling of a single thin–walled distensible vessel. Left: blood flow in the vessel as a function of $p_{\rm out}$. As long as $p_{\rm out} > p_{\rm e}$ (dark gray region), the flux in the tube increases as $p_{\rm out}$ is decreased. When $p_{\rm out} < p_{\rm e}$ (light gray region), the downstream portion of the tube enters into buckling instability and the flow reaches a plateau, becoming independent of $p_{\rm out}$. Right: 3D configuration assumed by the tube for $p_{out} = 10$ mmHg. A selected number of cross section shapes (black lines) are highlighted. Notice the very small dumbbell-shaped cross sections formed at the end of the vessel.

increases till $p_{\rm out} > p_{\rm e}$. When $p_{\rm out} = p_{\rm e}$, the downstream portion of the tube enters into buckling. The flow reaches then a plateau value and it does not depend any more on $p_{\rm out}$. This trend is in qualitative accordance with the predictions of the Starling resistor model. However, in this latter model only two situations are possible, fully patent or fully closed vessel cross section. The distensible behavior simulated in the present work is more complex, since the conductivities are consistently coupled with the transmural pressure. In Fig. 7(right), we show as an example the 3D configuration of the tube when $p_{\rm out} = 10$ mmHg. Notice the narrow deformed cross sections in the very downstream portion of the vessel where the low outlet pressure acts. A similar configuration was also observed in [45], where a more complex structural shell model coupled with fluid lubrication theory were used to simulate the experimental setting of the Starling resistor device (notice that in [45] the upstream and downstream cross sections of the tube are maintained fixed).

2.4. Computation of the conductivity vs. transmural pressure curve

The knowledge of the geometry of the deformed luminal cross section as a function of the pressure loads allows for computing the element conductivity from relation (3). In detail, we proceed as follows:

- if the deformed section remains circular, relations (12) explicitly give the radius of the blood-wall interface. The solution of problem (2) can be then found analytically, and yields the usual parabolic Poiseuille velocity profile [36], from which the conductivity can be straightforwardly computed by integrating (3);

- if the section is buckled, problem (2) is numerically solved with finite elements on a triangulation of the deformed section. Vessel conductivity is then obtained by 2D numerical quadrature of the integral (3). Observe that in our procedure, the buckled configuration is numerically computed only for a finite number of transmural pressure values. We then reconstruct a continuous conductivity curve by interpolation of such discrete values.

Tab. 1 summarizes the different expressions/techniques which give the conductivity parameter for thick and thin–walled ring elements, respectively.

	pre–buckling	post–buckling
thick–walled ring	$\sigma(\overline{p}) = \frac{\pi R_u^4}{8\mu}\left(1 + \frac{(1-\nu)}{E}B_1(\overline{p}) - \frac{(1+\nu)}{E}\frac{B_2(\overline{p})}{R_u^2}\right)^4$	/
thin–walled ring	$\sigma(\overline{p}) = \frac{\pi R_u^4}{8\mu}\left(1 + \frac{(1-\nu^2)}{\gamma E}(\overline{p} - p_{\mathrm{e}})\right)^4$	numerical solution see Sect. 2.3.2

Table 1: Summary of the different expressions and techniques to obtain the conductivity for thick and thin–walled ring elements. Only positive transmural pressure are considered for the thick–walled rings. The quantities B_1 and B_2 are the linear functions of the pressure loads defined in Sect. 2.3.1. Notice that here we have made explicit the dependence on the pressure indicator $\overline{p}$.

Fig. 8 depicts an instance of the computed vessel conductivity as a function of the transmural pressure considering a representative arteriole with $\gamma = 0.32$ and venule with $\gamma = 0.05$, both with $R_u = 40$ μm. We choose the Young modulus as discussed in Sect.2.3.1 and we set $p_{\mathrm{e}} = 15$ mmHg. The red curve with circular markers represents the conductivity parameter of the arteriole, the continuous blue curve the conductivity of the venule. The dashed blue curve in the region of negative transmural pressures represents, for comparison, the conductivity of the venule obtained from the second relation in

Tab. 1 (thin–walled ring) considering a circular cross section with the same area of the non-circular deformed geometry.

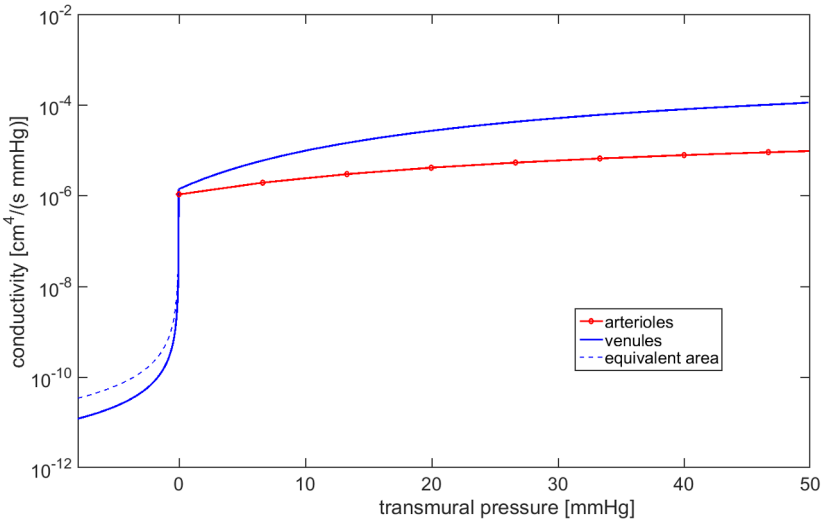

Figure 8: Vessel conductivity curve (log scale) plotted against the transmural pressure obtained for a representative arteriole (red continuous curve) and venule (blue continuous curve) with radius $R_d = 40$ μm. The external pressure is set to $p_e = 15$ mmHg, the Young modulus is chosen as discussed in Sect.5.2. The blue dotted curve represents the conductivity for a circular cross section with the same area of the buckled configuration at the same value of transmural pressure. Significant discrepancies arise as p_t decreases in the negative half–plane.

Notice how this latter curve significantly differs from the one obtained with the non–circular geometry, especially in the critical area around the onset of the buckling. This motivates us to the explicit computation of the buckled geometry.

2.5. Recovery of the unloaded configuration

We conclude the description of the model for a vessel element by dealing with the problem of recovering the unloaded configuration. We assume that the vessel configurations obtained from experimental measurements are circular. Since they do not correspond, in general, to unloaded conditions (configuration II or IV in Fig. 3), we have to solve an inverse problem, whose unknowns are the unloaded configuration itself and the stress field under which the measured deformed configuration is in equilibrium. Let

$$[R_d, h_d] = \mathcal{S}(R_u, h_u; p, p_e) \tag{18}$$

be the generic expression of the structural operator, corresponding to the thick or thin–walled ring models (direct problem). If the undeformed configuration were known, the operator $\mathcal{S}$ would compute the measured geometry under given pressure loads. In this context, we have to solve the inverse problem, where the unknowns are the unloaded configuration and the stress field under which the measured deformed configuration is in equilibrium. As, in general, the operator $\mathcal{S}$ cannot be analytically inverted, we resort to the fixed–point procedure described in Algorithm 1.

Algorithm 1 : computation of the undeformed geometry

given R_{d}, h_{d}, $p_{\mathrm{l}}, p_{\mathrm{e}}$;
fix toll, ω_r, $k_{\max}$;
set k=0, $R_{\mathrm{u}}^{(0)}$=R_{d}, $h_{\mathrm{u}}^{(0)}$=h_{d};
while **and**(err $\geq$ toll, $k \leq k_{\max}$) **do**
  $X^{(\mathrm{k})} = \mathcal{S}(R_{\mathrm{u}}^{(\mathrm{k})}, h_{\mathrm{u}}^{(\mathrm{k})}; p_{\mathrm{l}}, p_{\mathrm{e}})$;
  $u^{(\mathrm{k})} = X^{(\mathrm{k})} - R_{\mathrm{u}}^{(\mathrm{k})}$;
  $R_{\mathrm{u}}^{(\mathrm{k}+1)} = \omega_r(R_{\mathrm{d}} - \mathrm{u}^{(\mathrm{k})}) + (1-\omega_r)R_{\mathrm{u}}^{(\mathrm{k})}$;
  compute $h_{\mathrm{u}}^{(\mathrm{k}+1)}$ from $R_{\mathrm{u}}^{(\mathrm{k}+1)}$ using wall incompressibility;
  err= $\|R^{(\mathrm{k}+1)} - R_{\mathrm{u}}^{(\mathrm{k})}\| / \|R_{\mathrm{u}}^{(\mathrm{k})}\|$;
  $k = k + 1$;
end while
R_{u}=$R_{\mathrm{u}}^{(\mathrm{k})}$, $h_{\mathrm{u}} = h_{\mathrm{u}}^{(\mathrm{k})}$

Algorithm 1 is similar to the ones proposed in the computational frameworks of [19, 46] in biomedical applications, with the introduction in the present case of a relaxation parameter ω_r. We have found in our computations that the number of iterations that are actually needed to converge is related to the parameter values, being in particular affected by the wall thickness-to-radius ratio and by the Young modulus basal value.

An example of the application of Algorithm 1 is the following. We start from the deformed geometry (configuration I) of an arteriole with circular cross section of radius $R_{\mathrm{d}} = 40$ μm, thickness $h_{\mathrm{d}} = 12.8$ μm, luminal pressure $p_{\mathrm{d}} = 40$ mmHg and external pressure $p_{\mathrm{e,d}} = 15$ mmHg (data from [34]). The Young modulus is modeled as in Sect. 2.3.1. From Algorithm 1, we obtain the unloaded configuration II represented in Fig. 9(left). Convergence till tolerance 10^{-6} is achieved after less than 20 iterations with $\omega_r = 0.3$. To

give an idea of the importance of reconstructing the unloaded configuration, we also compute configuration III (zero transmural pressure) from II setting $p = p_e = 15$ mmHg and configuration IV, which is the unloaded geometry computed from I using the thin–walled ring model (see again Fig. 9(left)). Observe that configuration IV is only considered for comparison purposes, since the use of the thin–walled ring model is not appropriate with the present value $\gamma = 0.32$.

We now apply to configurations I to IV, successively considered as undeformed geometries, the loads $p = 20$ mmHg and $p_e = 10$ mmHg. In Fig. 9(right), we show the resulting deformation and hoop stress fields.

A significant discrepancy in the stress fields is evident. Configuration I yields stresses which differ of about 1 mmHg with respect to the ones from configuration II (measured vs. unloaded geometry). More significant differences arise if configuration IV is used instead of II (thin vs. thick structure model). The discrepancies are an increasing function of the magnitude of the transmural pressure, of the individual internal and external pressures, and of the Young modulus (data not reported). Tab. 2 summarizes the geometrical features of each configuration and the percentage difference in results with respect to the ones obtained from configuration I. We conclude this section by noting that in the present work we do not consider the existence of pre–stresses (residual–stresses). It is well know that, if cut radially, vessels spring

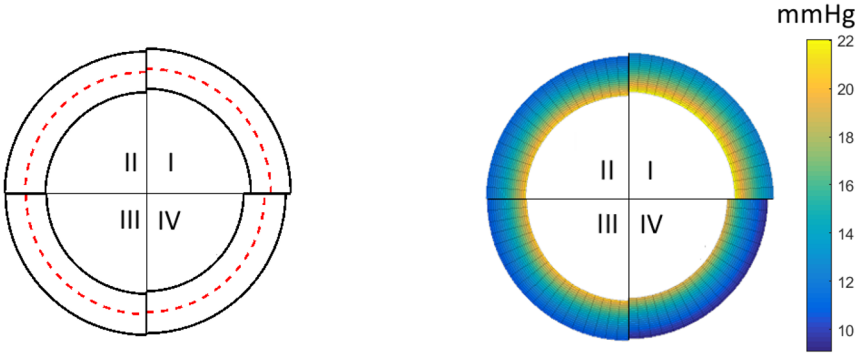

Figure 9: Left: configurations I-IV used as unloaded geometries in the numerical experiment described in the text. The red dotted-line represents the mean radius of the configuration. Right: distribution of the hoop stress obtained loading configurations I to IV with $p = 20$ mmHg and $p_e = 10$ mmHg. Stresses color code the corresponding deformed configurations.

		Configuration			
Row		I	II	III	IV
1	R [μm]	40	38.9	38.5	38.0
2	$\Delta^r R$ [%]	/	2.8	3.5	5.3
3	h [μm]	12.8	13.1	13.2	13.5
4	$\Delta^r h$ [%]	/	-2.2	-3.0	-5.6
5	$\Delta^r \sigma_T$ [%]	/	9.1	11.9	19.5

Table 2: Geometrical data and stress values for configurations I to IV and percentage variations with respect to values of configuration I. Data refer to the example presented in Sect. 2.5. Row 1 and 3: mean radius and wall thickness of the initial configurations as in Fig. 9(left); rows 2 and 4: percentage variation of the mean radius and wall thickness in the deformed configuration as in Fig. 9(right); row 5: percentage variation of the hoop stress σ_T at the mean radius of the deformed configuration as in Fig. 9(right). The percentage variation is defined as $\Delta^r G := (G - G_d)/G_d$.

open releasing the residual stress and approaching the zero-stress state which is a circular sector [3]. This aspect is rather delicate and deserves further future analysis.

3. Extension to a network of microvessels

We now consider the study of the fluid field in a complete compliant microcirculatory network, organized into incoming arterioles, an intermediate capillary bed and draining venules. Referring to Fig. 1, the network $\mathcal{T}$ is split into N_c vessels $\mathcal{V}$, such that $\mathcal{T} = \bigcup_{i=1}^{N_c} \mathcal{V}_i$. Each vessel $\mathcal{V}_i$, in turn, is partitioned into N_e^i short consecutive elements $\mathcal{E}^i$, such that $\mathcal{V}_i = \bigcup_{j=1}^{N_e^i} \mathcal{E}^{i,j}$. Notice that each element in a vessel has its own cross section area and the number of elements for each vessel may vary but it has its own cross section area. Denoting by $\Omega_f^{i,j}$ the luminal space of the element $\mathcal{E}^{i,j}$, the fluid domain is given by $\Omega_{\mathcal{F}} = \bigcup_{i=1}^{N_c} \left(\bigcup_{j=1}^{N_e^i} \Omega_f^{i,j} \right)$.

Junctions between vessel elements and different vessels are simply modeled as nodal points. Let N_{int} be the number of junction nodes. For each node $n_k, k = 1, \ldots, N_{\text{int}}$, we denote by I_k the set of elements which converge in that node. Moreover, we denote by I_k^- the subset of I_k for which n_k is the first endpoint of the element, *i.e.*, an element belongs to I_k^- if its local axis coordinate is such that $z = 0$ in n_k. Similarly, we denote by I_k^+ the subset of I_k for which n_k is the second endpoint of the element, *i.e.*, an element

belongs to I_k^+ if its local axis coordinate is such that $z = L$ in n_k. At each node $n_k, k = 1, \ldots, N_{\text{int}}$, we impose continuity of pressure and conservation of flow (analogue of the electric Kirchhoff's law)

$$\sum_{i,j \in I_k^-} -Q^{i,j} + \sum_{i,j \in I_k^+} Q^{i,j} = 0. \tag{19}$$

At the inlet and outlet nodes n_{in} and n_{out} (physiologically, more than one inlet/outlet can be present in the network, for a total of N_{bdr} boundary nodes), we can apply inlet and outlet pressure values (that is, we impose an overall pressure drop, as in the simulations presented in this work), or an inlet flux and an outlet pressure (or viceversa).

4. Solution procedure

4.1. Model summary

Gathering all the above points, we obtain a nonlinear boundary value system of PDEs in the compliant domain $\Omega_{\mathcal{F}}$. Summarizing, we must solve the following

Problem 1. (Blood Flow Model in Compliant Microvessels): given the connectivity of $\mathcal{T}$, the external pressure, the unloaded configuration and the mechanical properties of the vessels (including the conductivity laws), find the piecewise constant function Q satisfying conditions (19) and the continuous–piecewise linear function p such that in each element it holds

$$\frac{dQ}{dz} = 0, \qquad Q = -\sigma(\overline{p})\frac{dp}{dz}, \tag{20}$$

where the conductivity $\sigma(\overline{p})$ is determined as summarized in Tab. 1. Problem 1 represents a system of nonlinear PDEs on the network graph.

4.2. Numerical approximation

To approximate the solution of Problem 1, it is convenient to think that its discrete counterpart stems from the adoption of a primal mixed finite element [47]. In this framework, $\mathcal{T}$ represents the "triangulation" of the domain, with elements $\mathcal{E}$. Specifically focusing on the case of prescribed inlet

and outlet pressures, we introduce the finite dimensional spaces (see [48] for a similar procedure, albeit in a different context):

$$\begin{aligned} W_h &:= \{w_h \in L^2(\Omega_{\mathcal{F}}) : w_{h|_{\Omega_f}} \in \mathbb{P}_0(\Omega_f),\, \forall\, \Omega_f \subset \Omega_{\mathcal{F}}\}, \\ V_{h;(g_1,g_2)} &:= \{v_h \in C^0(\Omega_{\mathcal{F}}) : v_{h|_{\Omega_f}} \in \mathbb{P}_1(\Omega_f),\, \forall\, \Omega_f \subset \Omega_{\mathcal{F}}, \\ &\qquad v_h(n_{in}) = g_1, v_h(n_{out}) = g_2\}. \end{aligned} \tag{21}$$

In Fig. 10, we show the shape function $v_{h,i} = v_{h,i}(z) \in V_{h;(g_1,g_2)}$ relative to node i. Notice that functions belonging to $V_{h;(g_1,g_2)}$ are: 1) globally continuous on the network; 2) linear on each element in $I_i^+ \cup I_i^-$; 3) such that $v_{h,i} = \delta_{i,r}$, $r = 1, 2, \ldots, N_{tot}$, where we have set $N_{tot} = (N_{\rm int} + N_{\rm bdr})$.

In order to introduce the discrete weak formulation of Problem 1, we let $\mathcal{R}(\overline{p}) = 1/\sigma(\overline{p})$ be the non–negative tube resistance per unit length (observe that $\sigma(\overline{p}) > 0$ in the physiological range) and $\forall\, Q_h, w_h \in W_h, v_h \in V_{h;(g_1,g_2)}$, $p_h \in V_{h;(p_{in},p_{out})}$, we define

$$A(Q_h, w_h; p_h) = \int_{\mathcal{T}} \mathcal{R}(p_h)\, Q_h\, w_h\, dz, \quad B(v_h, Q_h) = \int_{\mathcal{T}} \frac{dv_h}{dz}\, Q_h\, dz. \tag{22}$$

The FE discretized version of Problem 1 reads:

Problem 2: find $(Q_h, p_h) \in (W_h \times V_{h;(p_{in},p_{out})})$ such that, $\forall w_h \in W_h, \forall v_h \in V_{h;(0,0)}$

$$\begin{aligned} &A(Q_h, w_h; p_h) + B(p_h, w_h) = 0, \\ &B(v_h, Q_h) = 0 \end{aligned} \tag{23}$$

Problem 2 is still non-linear, due to the dependence of the conductivity on the pressure in the FSI problem. We linearize it by introducing the fixed point iteration detailed in Algorithm 2. Notice that in order to achieve convergence in the internal iteration a relaxation procedure is necessary. We have empirically observed that satisfying a convergence criterion on the pressure but also on the fluxes improves the overall solution.

We observe that the solution of system (24) can be carried out by formal elimination of the flux variables as a function of the sole pressure variables. This procedure yields at each internal iteration the linear algebraic system: find the vector of nodal pressures $P \in \mathbb{R}^{N_{tot}\times 1}$ such that

$$\mathcal{M} P = F, \tag{25}$$

where $F \in \mathbb{R}^{N_{tot}\times 1}$ is the right–hand side and $\mathcal{M} \in \mathbb{R}^{N_{tot}\times N_{tot}}$ is the stiffness matrix.

Algorithm 2 : fixed point iteration to compute the fluid-dynamical field on the network

given p_{start};
fix toll, ω_p, ω_Q, $k_{\max}$;
set $p_h^{(0)} = p_{\text{start}}$, k=0;
while **and**(err $\geq$ toll, k $\leq$ $k_{\max}$) **do**
compute $\overline{p}_h^{(k)}$= **mean**($p_h^{(k)}$) on each vessel;
compute for each vessel the cross section geometry under the load $\overline{p}_h^{(k)}$;
update $\sigma_h^{(\text{k})} = \sigma_h(\overline{p}^{(\text{k})})$;
solve the following linearized version of Problem 2

$$\begin{aligned} &A(Q_h^{(k+1)}, w_h; \overline{p}_h^{(k)}) + B(p_h^{(k+1)}, w_h) = 0, \\ &B(v_h, Q_h^{(k+1)}) = 0 \end{aligned} \tag{24}$$

set $p_h^{(\text{k}+1)} = \omega_p p_h^{(\text{k}+1)} + (1-\omega_p) p_h^{(\text{k})}$;
set $Q_h^{(\text{k}+1)} = \omega_Q Q_h^{(\text{k}+1)} + (1-\omega_Q) Q_h^{(\text{k})}$;
err= $\max\{\|Q_h^{(\text{k}+1)} - Q_h^{(\text{k})}\|/\|Q_h^{(\text{k})}\|,\ \|p_h^{(\text{k}+1)} - p_h^{(\text{k})}\|/\|p_h^{(\text{k})}\|\ \}$;
k=k+1;
end while
set $Q_h = Q_h^{(k)}, p_h = p_h^{(k)}$.

To provide an example of the resulting equations, we refer again to Fig. 10, omitting for brevity the k superscripts of the internal iteration procedure. We explicitly write the rows involving node n_i, with converging vessel elements $\mathcal{E}^l, \mathcal{E}^k, \mathcal{E}^m$ (here, again for brevity, we have used a shortened notation for vessel elements):

$$\mathcal{R}_l(\overline{p}_l)\, Q_l L_l + (p_i - p_{i-1}) = 0, \tag{26}$$
$$\mathcal{R}_k(\overline{p}_k)\, Q_k L_k + (p_{i+1} - p_i) = 0, \tag{27}$$
$$\mathcal{R}_m(\overline{p}_m)\, Q_m L_m + (p_{i+2} - p_i) = 0, \tag{28}$$
$$-Q_l + Q_k + Q_m = 0. \tag{29}$$

Notice that we make implicit use of the fact that functions in $V_{h;(g_1,g_2)}$ are piecewise linear continuous over $\mathcal{T}$, so that they ensure the automatic satisfaction of the pressure coupling condition. The value of the pressure for all

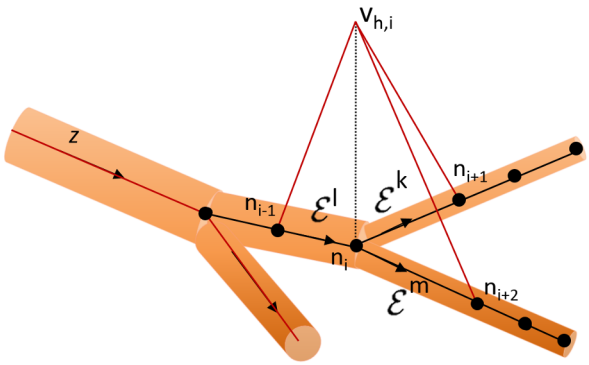

Figure 10: Bifurcation of the network including the joining node n_i and the converging vessel elements $\mathcal{E}^l, \mathcal{E}^k, \mathcal{E}^m$. On each element, the arrow indicates the positive direction of the local z axis. This choice implies that $I_i^+ = \{l\}, I_i^- = \{k, m\}$. The linear "web–like" shape function $v_{h,i} \in V_h$ is also represented.

the vessels converging in the node n_i is thus uniquely identified by p_i. Substituting Eq. (26),(27),(28) (generalized Ohm's laws) in Eq. (29) provides a reduced relation in the sole nodal pressure unknowns. Gathering together the resulting relations for all the internal nodes gives a system of the type (25).

5. Numerical simulations

5.1. A practical instance of "measured" geometry of a microcirculatory network: the case of eye retina vessels

The methodology described in the previous sections can address the solution of general unstructured networks. In this work we specifically focus on a model which represents the structure of the eye retina microcirculation. This is a so-called terminal district, meaning that it has a single input (the central retinal artery) and a single output (the central retinal vein). We observe, however, that in other microcirculatory districts it is normal to have a redundancy of inputs and outputs pathways for blood flow. This latter issue is very delicate, since there is a big question on how to enforce boundary conditions in every terminal branch, in lack of data, and we are not dwelling into it in the present work. We consider arteriolar and venular networks with a mirrored organization, according to the structure proposed in [34] for the same district. In general, the topological organization of the venular network

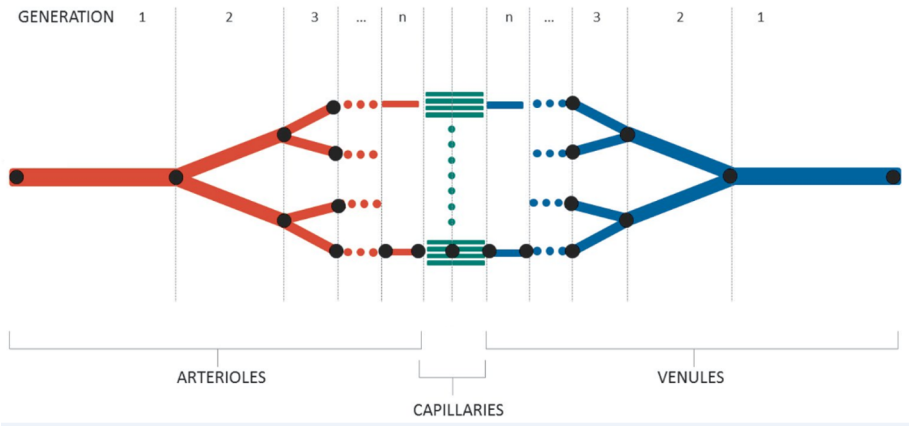

Figure 11: Schematic representation of the structure of the vascular networks considered for the numerical simulations. The generation numbers denotes the hierarchical position of a certain vessel in the network. For simplicity, all the vessels are represented as having the same diameter, but asymmetric networks are considered as well.

is recognized to be similar to that of the arteriolar network [49], although the venule network organization has not been studied as extensively as the one on the arterial side. Venules are generally more numerous than arterioles at the same level of the network (we do not keep into account this point) and the diameter of venous vessels is substantially greater than the arteriole at the same level of the network (we consider here a diameter of the venules 30% greater than the one of the corresponding arterioles). Terminal arterioles and venules are connected one-to-one through four parallel capillaries.

In Fig. 11, we provide a schematic representation of the structure of the vascular networks we consider. Whilst representing an evident idealization of the real anatomy, this model allows us to carry out a more systematic discussion on the results, filtering out the effects of the local irregularity and complexity of the geometry.

Arterioles and venules are supposed to branch with Y–shaped bifurcations and the vessel diameters at the branching points are defined according to a modified Murray's Law [50]: letting D_f be the diameter of the larger (father) vessel in a bifurcation and D_{d_1}, D_{d_2} the diameters of the smaller (daughter) vessels, the following relation is assumed

$$D_f^m = D_{d_1}^m + D_{d_2}^m, \tag{30}$$

where $m = 2.85$ is the fractal bifurcation exponent. We assume, as described

in [14], that the daughter vessels have (possibly different) diameters, given according to

$$D_{d_1} = c_{d_1/f} D_f, \qquad D_{d_2} = D_f (1 - c_{d_1/f}^m)^{1/m}, \tag{31}$$

where $c_{d_1/f}$ is a given proportionality coefficient and where D_{d_2} has been obtained enforcing (30). The generation of the network is continued as long as the vessel diameter is greater than 6 μm. Observe that $c_{d_1/f} = 2^{-1/m} = 0.784$ yields a symmetric dichotomic network with a constant number of branchings leading from the root to each leaf. The length L of each vessel is chosen to be a fractal function of the diameter, according to $L = 7.4 D^{1.15}$, as in [34]. Capillaries have diameter 6 μm and length 500 μm [34].

In Fig. 12 we show an example of network obtained setting $c_{d_1/f} = 0.7$. Notice that, whilst the above described fractal networks do not possess, *per se*, a spatial structure, we endow the network of 3D geometrical coordinates by orienting in the space each daughter branch with respect to the father with elevation and azimuthal solid angles chosen in a range which respects anatomical features. This procedure, on the one side, facilitates the visualization of the network and its physical fields. On the other, more importantly, this allows to locally modify vessel properties or external conditions in a certain 3D spatial region to reproduce physiological and pathological alterations of the baseline values.

Assessment of the in silico generated networks: comparison with experimental measures. To assess the fact that the above considered networks can compute physiologically coherent fluid-dynamical fields, we compare the blood flow we obtain from model simulation with the experimental measures in humans performed by different authors in the same diameter range. The external pressure is set to $p_{\mathrm{e}} = 15$ mmHg, corresponding to the intraocular pressure of a healthy subject. The results are shown in Fig. 13, which favorably compares volumetric blood fluxes. Blood velocities (not represented) are also coherent.

5.2. Physical and numerical parameters

If not otherwise specified, simulations are run considering coupled arteriolar and venular networks geometrically described on each side as in Sect. 5.1 with $c_{d_1/f} = 0.7$. This value yields a non-symmetric dichotomic network whose anatomical features are relevant to the retinal circulation [14]. The

other parameters are chosen as follows according to the simulation results carried out by Takahashi [34], which were able to reproduce physiologically coherent velocity and flow fields. We set the network inlet pressure to 42 mmHg and the outlet pressure to 18 mmHg, respectively. The inlet arteriole has radius equal to 62μm, the outlet venule equal to 72.5 μm. We set γ equal to 0.32 for arterioles and 0.05 for venules, which are reasonable values according to the metadata collected in [39]. The first half length of each capillary is considered to belong to the arteriolar network, and thus described as a thick–walled ring, with $\gamma = 0.2$. The second half length is considered to belong to the venular network, and thus is described as a thin–walled ring, with $\gamma = 0.08$.

Blood viscosity is described according to the model of [51], where it is

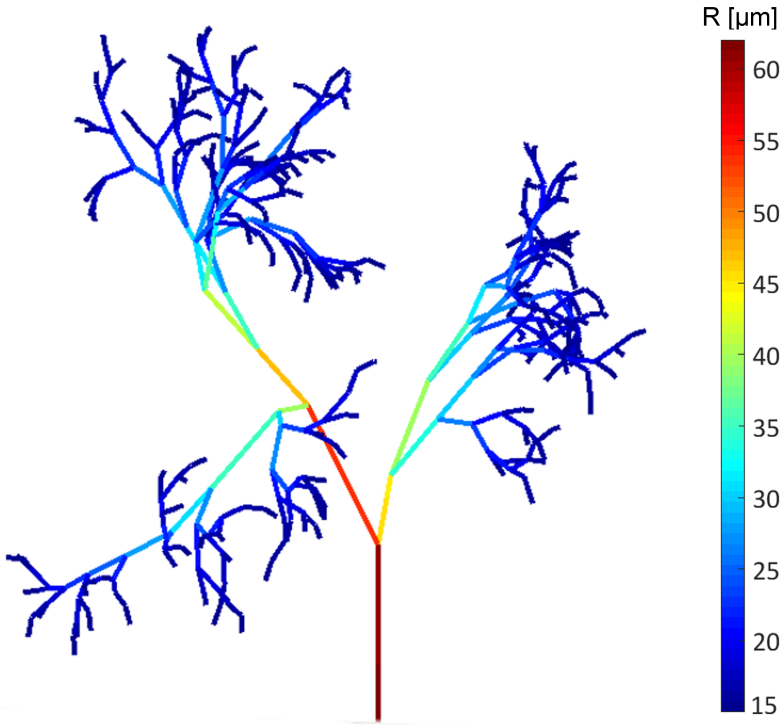

Figure 12: Example of a network (arterial side only) considered in the following simulations, represented in the pseudo–3D space. The network is asymmetric ($c_{d_1/f} = 0.7$), as is evident from the colors mapping the value of the radii and the different branching structure. To improve the readability of the figure, the smallest vessels are not shown.

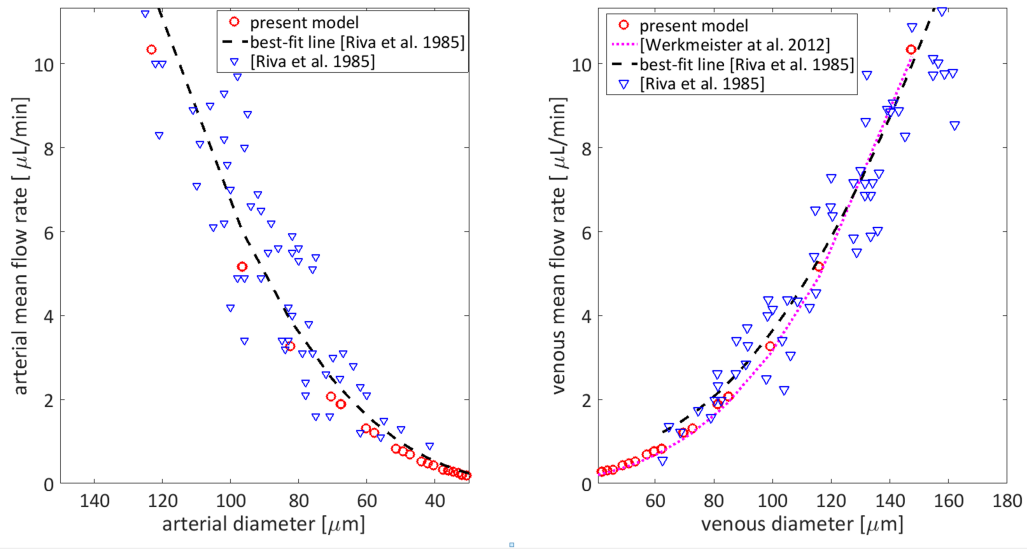

Figure 13: Comparison of blood flow computed by the present model on a network generated by fractal branching and experimental data measured in humans by different authors.

considered to be a function of plasma viscosity ($= 1cP$), blood hematocrit ($= 45\%$) and vessel diameter. In this representation, the viscosity decreases as the vessel diameter decreases till a diameter of about 40 μm, then it starts to increase again with high steepness for smaller vessels. We choose to account for non–circular shapes by using the concept of hydraulic diameter defined as four times the ratio between the vessel cross sectional area and the wetted perimeter of the cross-section [52].

For computation purposes, each vessel is then split into equal–sized elements with radius and wall thickness equal to that of the vessel itself. The undeformed geometry is recovered according to the Algorithm 1. Notice that in this latter configuration the radius of elements of the same vessels may be different due to nonuniform pressure load.

We have studied the influence on the results of the number of element into which each vessel is partitioned. This difference is extremely small when considering the physiological range of typical external and internal blood pressures. It is clear that, were the external pressure be significantly higher than the internal one, using a greater number of elements -eventually with an appropriate adaptive refinement - allows to obtain a more accurate description of the buckling phenomenon. In the following, we set $N_e = 3$ in

each vessel.

5.3. Simulation results

In the following, we present the results obtained in different test cases which highlight significant network behaviors.

Pressure field in the network as a function of the interstitial pressure. We computationally solve the mathematical model choosing a uniform interstitial pressure. We set successively $p_e = [15, 18, 20, 22]$ mmHg. observe that, in the application we have in mind, the eye retina microcirculation, We notice that, in this context, the interstitial (external) pressure essentially corresponds to the so–called intraocular pressure (IOP), which is a parameter largely independent from the systemic blood pressure. Normotensive individuals (healthy or medicated) may present elevated IOP values, as well as hypertensive individuals may present normal values of IOP. We refer to our work [53] for a comprehensive study of the sensitivity with respect to the blood flow boundary conditions in a generic microcirculatory network.

For ease of presentation, in the following we report separately the results for arteries and veins, even if the simulations are run on the coupled model. We have binned the vessel into classes according to their reference diameters. Class boundaries are obtained by partitioning the range between the minimum and maximum diameter into 20 classes using log10 spacing. Class 1 corresponds to larger vessel, 20 to smaller ones. For each class, we plot the bars whose heights represent the relative number (with respect to the total number of arteries and veins, respectively) of vessels displaying an average pressure in the color–coded range. Colored continuous curves link the height of the bars belonging to the same pressure range. Fig. 14 shows the histogram plots for arteries, Fig. 15 for veins. Observe as, for increasing external pressure, peaks for each pressure range shift towards smaller vessels (larger vessels in the venular network), thus indicating a global increase in blood pressure. Lower pressure ranges progressively tend to disappear. This phenomenon is to be ascribed to the presence of buckled vessels in veins. In the two bottom panels of Fig. 15 we also observe a much more sharp compartmentalization of lower pressure ranges in class 1. Again, this phenomenon is to be ascribed to the presence buckled vessels. This is also the cause of the larger spreading in pressure ranges attained over the diameter classes for increasing p_e. These differences are more evident in the step p_e=20 to 22 mmHg (p_e=18 to 20 mmHg for the venous network) than in the previous

steps. Elbow–like turns or "holes" in the enveloping curves are instead due to the asymmetry of the network and the specific bin classification of each vessel.

Observe that the pressure shift in the network is due to the concurrence of several mechanisms. The networks we consider in our simulations have a single input/output vessel. This implies that the network could be reduced to an equivalent resistive vessel. This lumped vessel behaves similarly to a Starling resistor (elastic-walled version of Hagen-Poiseuille flow). Typically, when a uniform external pressure is applied to a vessel, only the very last part of it participates in the non-axisymmetric buckling. As the external pressure increases, the buckling point moves towards the very end of the vessel and a stronger pressure drop occurs in the buckled vessels. This behavior is also observed in experiments (see also *e.g.*, Fig.8.5 in [22] for a long single vessel). When one comes back to the topologically organized network, this amounts to say that the buckling will always occur in the very last vessels.

Impact of boundary conditions

We examine the impact of the boundary conditions on the network behavior. A sensitivity analysis on this aspect had already been object of study in our recent works [15] and [53]. In the first work we performed this type of analysis on a large unstructured rigid network, while in the second we focused on a simple bifurcation of converging or diverging compliant vessels. Here, we consider the large compliant network described in Sect. sec:geo-ne and we monitor how the flow rate varies with the overall pressure drop applied between the upstream and downstream ends of the network. To do this, we keep the inlet pressure fixed at 40 mmHg and we progressively decrease the outlet pressure. The flow is thus driven by "downstream suction". We carry out this analysis for external pressure equal to 15 and 20 mmHg, respectively. If the external pressure is lower than the outlet pressure, then all the vessels in the network are in pre–buckled axi-symmetric configuration. As the external pressure approaches the value of the pressure in a vessel, this adds compressive load on the vessel wall. However, as long as the compression remains small, the tube resistance changes minimally. This results in an approximately linear pressure-drop/flow rate relationship (see Fig. 16). As the compressive loads further increases, the flow rate/pressure drop curve saturates, till when the most downstream vessel, where the pressure is the lowest, enters into buckling. At this point, a net increase of flow resistance occurs. Notice that for $p_e = 15$ mmHg this corresponds to a pressure drop

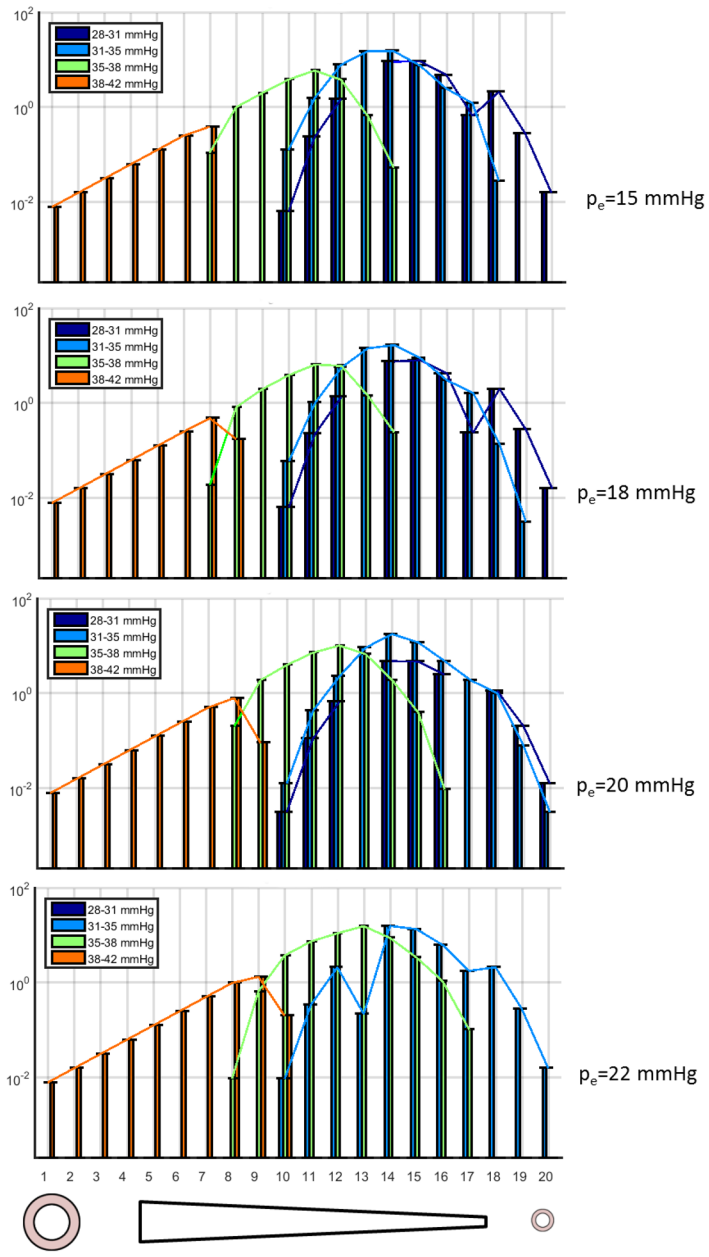

Figure 14: Histogram plots for relative frequencies of blood pressure in the arterial part of the network binned according to diameter class. Colored continuous curves link the height of the bars belonging to the same pressure range.

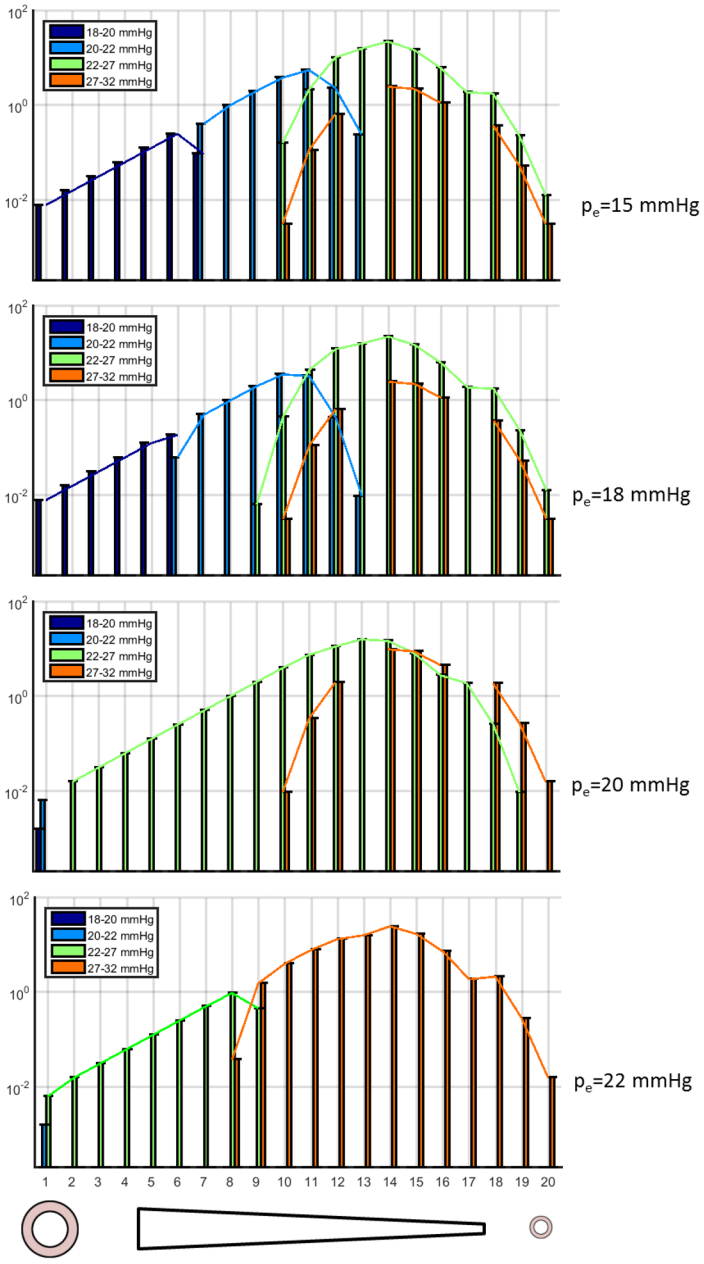

Figure 15: Histogram plots for the relative frequencies of pressures in the venous part of the network binned according to diameter class. Colored continuous curves link the height of the bars belonging to the same pressure range.

of 25 mmHg, while for $p_e = 20$ mmHg this corresponds to a pressure drop of 20 mmHg. From this point on, a "negative effort dependence "appears in the flow rate/pressure drop , where an increase in the driving force/pressure drop leads to a reduction in flow rate due to the higher resistance. Increasing the external pressure reduces the pressure drop range for which the flow is increasing, shifting the curve to the left. A similar behavior was obtained for the model of Starling resistor proposed in [22]. In this work, the authors analyzed (between the others) the flow rate in a single long vessel for varying outlet pressure. The more complex structural model they used also allowed to reveal the hysteretic behavior of the vessel when the external load is increased and then decreased. This latter point cannot be described with the present simplified structural model.

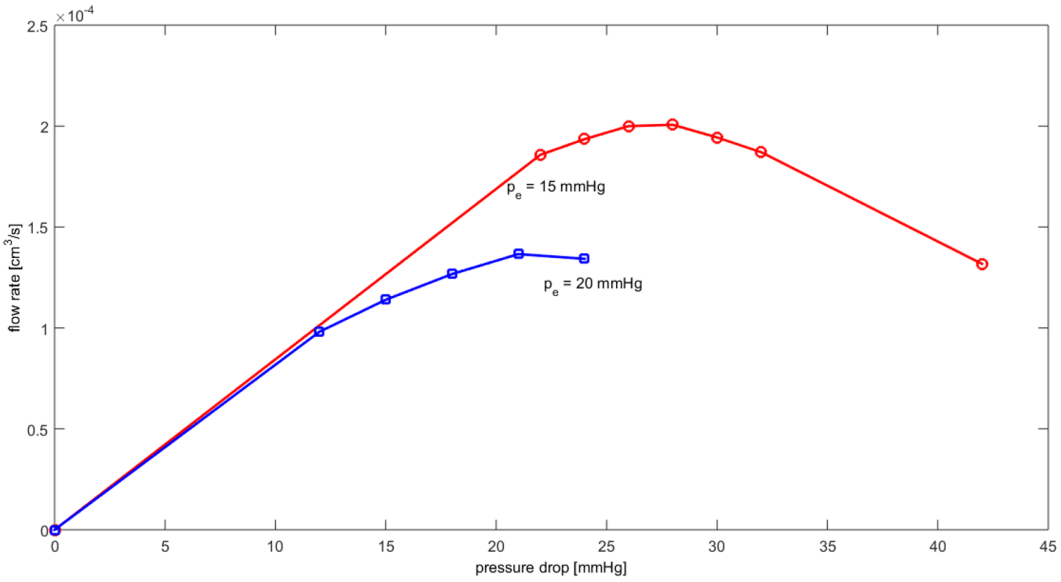

Figure 16: Flow rate as a function of the overall pressure drop applied between the upstream and downstream ends of the network. The inlet pressure is kept fixed at 40 mmHg and the outlet pressure is progressively decreased. The analysis is carried out for external pressure equal to 15 and 20 mmHg, respectively. Notice that for $p_e = 15$ mmHg the pressure drop of first buckling is 25 mmHg, while for $p_e = 20$ mmHg is 20 mmHg.

Network response to local increases of interstitial pressure. We artificially increase the external pressure to $p_e = 20$ mmHg (elsewhere being equal to 15 mmHg) in a delimited portion of the network, located at the interior of

a sphere with center in the venous post–capillary zone and radius chosen to include a sufficient number of vessels (gray–shaded region in Fig. 17(bottom row)). This setting simulates, for example, the presence of an edema. In Fig. 17, we plot color–coded net variation Δp of blood pressure in the arterial and venous networks along with a zoom of the affected regions. In Tab. 3 we report the maximal (with sign) percentage variation along the arteriolar and venular network of blood pressure, blood flux, cross section area and vessel resistance. Albeit no vessel properly enters into buckling instability due to the chosen parameters, a strong increase in resistance is observed in veins due to the combination of area variation and consequent high rise of blood viscosity, strongly diameter depended in that region. Observe also how blood pressure and flow variations are instead similar, this being connected to the continuity conditions enforced at the artero-venous interfaces. This generates strong flux diversion and "flux stealing" from other vessels [53, 54], localized in the four or five generations surrounding the sphere. Observe that, whilst no arterial vessel is actually included in the sphere, there exists a region of the arterial network which is also affected by perturbations.

	arterioles	venules
mean blood pressure	+6.46 %	+7.10 %
flow rate	-15.07 %	-15.14 %
cross section area	-15.20 %	-55.47 %
conductance	-31.84 %	-91.64 %

Table 3: Maximal (with sign) percentage variations of the arteriolar and venular networks in the specified vessel parameters subsequent to a local increase of external pressure in the spherical region depicted in Fig. 17.

6. Conclusions

The ability of single body's organs to bring about large selective variations in the rate of blood perfusion relies on the sophisticated regulatory mechanisms of the peripheral circulatory districts. Blood flow regulation is obtained by variation of the vessel diameter, under the effect of both passive and active actions. In this work, we have focused our attention on the first set of mechanisms, investigating the role of geometrical and structural (the so-called "physical") factors in flow regulation. The key point in this process is compliance: elastic microvessels subject to mechanical loads undergo

deformations of their wall, altering the shape of the domain offered to blood and, ultimately, resistance to flow. This implies, in turn, a redistribution of the flow itself in the network.

The modeling strategy we have proposed in this work uses a simplified description of blood flow and vessel wall-to-flow interaction in order to make feasible computations on large networks. At the same time, important features - peculiar characteristic of these networks- are retained. Blood flow and pressure drop in each vessel element have been connected by a generalized Ohm's law including a conductivity parameter, function of the area and shape of the tube cross section. These latter have been determined in a consistent way by a thin or thick–wall structural model loaded by the internal and external pressure loads. A buckling model is considered in the case of venules, which can experience low/possibly negative values of transmural pressure.

Simulations carried out using the mathematical model show that globally increasing the external pressure causes a global increase in luminal pressure. This process is gradual till buckling occurs somewhere, typically at the outflow, in the venous district. At this point the process has a sort of discontinuity with a much more marked pressure increase. Locally increasing the external pressure, on the other side, has an influence which can be estimated to extend till four or five vessels generations away from the perturbed area. One important point emerges from the above results. Vessels of the same size may experience different intravascular pressure values due to their different location in the network. Hence, even though the vessels embedded in a certain tissue can be classified according to size or branching order, the hemodynamic phenomena which are associated with changes in intravascular pressure should be analyzed and interpreted with caution, especially when considering asymmetrically branching systems.

The present model can be used to investigate alterations in microcirculatory beds due to pathological conditions. Hyperglycemia in diabetes mellitus is known to cause important structural, biochemical and functional changes in the peripheral circulation [55]. Alzheimer's disease, atherosclerosis or vascular dementia can change vascular stiffness. Elevated systolic pressure (hypertension) increases the zero pressure lumen area and the buckling pressure, so that an hypertensive vessel is more likely to collapse than a normal one [56], with many possible hemodynamic consequences. To address these points in a proper way, the following issues should be taken into account in the future:

i) inclusion of a more realistic and detailed blood rheology. In our work [15], we have represented blood as a mixture of two fluids, plasma and red blood cells, considering the effects of red blood cell partition at the bifurcations and blood viscosity depending on vessel geometry and variable hematocrit. A similar approach could be extended without too many difficulties to the present model;

ii) inclusion of a more realistic model of capillary beds and coupling with the surrounding tissue. If, on the one side, capillaries show a pretty regular mesh–like organization almost ubiquitous in the body, on the other, it is not feasible to face their complete description. Dual mesh techniques as discussed in [57] for cerebral microvasculature can be used to study the dialog between the hemodynamic network and the surrounding tissue. Alternatively, homogenized models for porous media can also be used to effectively face this problem as done in [58] for pulmonary alveoli circulation;

iii) inclusion of "acute autoregulation" capabilities in arterioles, which actively respond to stimuli to maintain an adequate blood supply and nutrient delivery to tissue. This topic is naturally founded on having a disposal a model for blood–tissue interaction as described in point ii). Possible regulatory laws could be borrowed from the works by Ursino and co–authors (see, *e.g.*, [59] and references therein) in the case of compartmental models, and from the works by Arciero and co-authors (see, *e.g.*, [60, 61]) in the case of a simplified representative 1D/segment model of large/small arteries/veins and capillaries. In these works, the vasoactive response of the arterioles is modeled via "regulatory variables" which depend on myogenic and metabolic stimuli according to phenomenological laws. Similar approaches have been recently adopted to simulate vessel recruitment by David and co-authors (see, *e.g.*, [62] and references therein) for realistic network of the cerebral microcirculation, and by Secomb and co-authors (see, *e.g.*, [29] and references therein).

Appendix A. Numerical computation of the buckled cross section for $p_{\mathrm{t,cl}} < p_{\mathrm{t}} < p_{\mathrm{t,b}}$

The shape of the buckled cross section in the range $p_{\mathrm{t,cl}} < p_{\mathrm{t}} < p_{\mathrm{t,b}}$ is performed by numerically solving the boundary value problem (16) by means of

the Matlab function `bvp4c`. This function requires to provide an initial guess of the solution, an appropriate choice of which is of fundamental importance. As matter of fact, if the guess solution corresponds to a perfectly circular shape, the solver will stagnate on that same shape (see [21] for a similar observation). To kick in the instability, we provide a guess shape with a curvature which is a small perturbation (with parameter $\varepsilon \ll 1$) of the curvature of the reference circle of radius R_u, namely we set $\mathcal{K}_\varepsilon = \dfrac{1}{R_u}\left(1 + \varepsilon \cos \dfrac{s}{R_u}\right)$. We have found that the value of ε must be tuned accordingly to the imposed transmural pressure: the more buckled is the expected shape of the cross section, the more we need to use a strong perturbation in order to obtain a physically coherent solution. Alternatively, we have also tried - once we have computed the first buckled shape - to directly provide it to the solver as a guess and this also provided the correct solution. As a final remark, one should observe that, as already noticed by Fung in his book [3], there exists a conceptual parallel between the need of providing to the solver a guess shape which is not exactly circular -a need purely connected to start the numerical procedure- and the existence in nature of imperfections in the vessel (in the material composition, in the geometrical shape or in the load disposition) which actually trigger the instability.

Appendix B. Functional representation of the Young modulus. Whilst for large blood vessels, especially the carotid, much work has been done, based on experimental measures possibly supported by the use of mathematical models (see, *e.g.*, [3],[63]), there is a substantial paucity of data and models for the representation of the Young modulus in microvessels. Given these premises, if one considers for simplicity E=const, then relations (12) become linear in the pressure, but the corresponding relation transmural pressure vs. cross section area exhibits two non–physiological features: (i) concave form and (ii) absence of saturation at a maximal cross section area for high transmural pressures. It seems then necessary to use a more complex description than a constant, also in view of the different reaction to loads of the components of the vessel wall (collagen, elastin). In this work, we use a linear functional dependence of Young modulus with respect to transmural pressure. This relation is obtained by fitting data from the measurements obtained in [64] by wire myography in small deactivated arteries and veins of the rat mesenteric circulation. The computed steepness of the linear relation is such that the Young modulus passes from a basal value E_b at zero transmu-

ral pressure to roughly its double when the transmural pressure is increased to 50 mmHg. In the present example of application of the model to the retinal circulation, we set $E_b = 0.022$ MPa for arterioles and $E_b = 0.066$ MPa for venules (basal values chosen as in [65] for the same microcirculatory district). Analogous trends can be obtained also considering different sets of measurements, for example the ones in [63] for human coronary arteries.

Appendix C. Influence of the asymmetry degree of the network

To assess the influence of the asymmetry degree of the network, we consider four different networks with progressively increasing symmetry (that is, with increasing index $c_{d_1/f}$), till reaching a symmetric dichotomic network $c_{d_1/f} = 0.784$. In Tab. A.4, we report the values of different features of these networks (total number of vessels, min and max route distance of the leaves of the tree, total cross section and equivalent resistance of the network in the measured configuration) for the considered values of $c_{d_1/f}$. Shown data refer to the arterial side. The trend of the parameters is due to the increasing homogeneity of the network, which affects the relation between radius and vessel length, and to the constraint of not trespassing the minimum diameter. These elements combined together result into an equivalent resistance which is more than doubled passing from $c_{d_1/f} = 0.5$ to $c_{d_1/f} = 0.784$.

	Asymmetry index $c_{d_1/f}$				trend
Parameter	0.5	0.6	0.7	0.784	
total number of vessels	15252	12415	9664	8191	↘
min route distance [μm]	$1.65 \cdot 10^3$	$1.84 \cdot 10^3$	$2.36 \cdot 10^3$	$3.13 \cdot 10^3$	↗
max route distance [μm]	$1.23 \cdot 10^4$	$7.17 \cdot 10^3$	$4.49 \cdot 10^3$	$3.13 \cdot 10^3$	↘
total cross section [μm^2]	$9.65 \cdot 10^5$	$7.33 \cdot 10^5$	$5.85 \cdot 10^5$	$5.17 \cdot 10^5$	↘
eq. resistance [cm^3/s/mmHg]	$7.84 \cdot 10^{-7}$	$1.14 \cdot 10^{-6}$	$1.43 \cdot 10^{-6}$	$1.7 \cdot 10^{-6}$	↗

Table .4: Characteristic values of parameters of networks (arterial side only) generated by different degrees of asymmetry in branching (increasing symmetry moving to the right, 0.784=symmetry). The last column indicates the trend of each parameter for increasing symmetry. Data correspond to a minimal diameter of 6 μm, inlet pressure 40 mmHg, outlet pressure 20 mmHg (values chosen as in [34]).

[1] A. Pries, Microcirculation abnormalities: assessment techniques, Medicographia 25 (2003) 231–236.

[2] R. Tuma, W. Duran, K. Ley (Eds.), Microcirculation, Elsevier.

[3] Y. C. Fung, Biomechanics: Circulation, Springer Science & Business Media, 2013.

[4] L. Formaggia, A. Quarteroni, A. Veneziani (Eds.), Cardiovascular Mathematics: Modeling and Simulation of the Circulatory System, Springer–Verlag, Italy, 2009.

[5] A. Brunberg, S. Heinke, J. Spillner, R. Autschbach, D. Abel, S. Leonhardt, Modeling and simulation of the cardiovascular system: a review of applications, methods, and potentials, Biomed. Tech. 54 (5) (2009) 233–244.

[6] A. Quarteroni, A. Veneziani, C. Vergara, Geometric multiscale modeling of the cardiovascular system, between theory and practice, Computer Methods in Applied Mechanics and Engineering 302 (2016) 193–252.

[7] D. Goldman, Theoretical models of microvascular oxygen transport to tissue, Microcirculation 15 (8) (2008) 795–811.

[8] M. Ursino, C. A. Lodi, A simple mathematical model of the interaction between intracranial pressure and cerebral hemodynamics, J. Appl. Physiol. 82 (4) (1997) 1256–1269.

[9] M. Ursino, C. A. Lodi, Interaction among autoregulation, CO_2 reactivity, and intracranial pressure: a mathematical model, Am. J. Physiol. Heart. Circ. Physiol. 274 (5) (1998) H1715–H1728.

[10] G. F. Ye, T. W. Moore, D. G. Buerk, D. Jaron, A compartmental model for oxygen-carbon dioxide coupled transport in the microcirculation, Ann. Biomed. Eng. 22 (5) (1994) 464–479.

[11] J. C. Arciero, B. E. Carlson, T. W. Secomb, Theoretical model of metabolic blood flow regulation: roles of atp release by red blood cells and conducted responses, Am J Physiol Heart Circ Physiol 295 (4) (2008) H1562–H1571.

[12] S. Fantini, Dynamic model for the tissue concentration and oxygen saturation of hemoglobin in relation to blood volume, flow velocity, and

oxygen consumption: Implications for functional neuroimaging and coherent hemodynamics spectroscopy (chs), Neuroimage 85 (2014) 202–221.

[13] T. K. Roy, A. R. Pries, T. W. Secomb, Theoretical comparison of wall-derived and erythrocyte-derived mechanisms for metabolic flow regulation in heterogeneous microvascular networks, Am. J. Physiol. Heart. Circ. Physiol. 302 (10) (2012) H1945–H1952.

[14] T. Takahashi, Microcirculation in fractal branching networks, Springer, 2014.

[15] P. Causin, G. Guidoboni, F. Malgaroli, R. Sacco, A. Harris, Blood flow mechanics and oxygen transport and delivery in the retinal microcirculation: multiscale mathematical modeling and numerical simulation, Biomech. Model. Mechanobiol. (2015) 1–18.

[16] J. Reichold, M. Stampanoni, A. L. Keller, A. Buck, P. Jenny, B. Weber, Vascular graph model to simulate the cerebral blood flow in realistic vascular networks, Journal of Cerebral Blood Flow & Metabolism 29 (8) (2009) 1429–1443.

[17] A. A. Linninger, I. Gould, T. Marinnan, C.-Y. Hsu, M. Chojecki, A. Alaraj, Cerebral microcirculation and oxygen tension in the human secondary cortex, Annals of biomedical engineering 41 (11) (2013) 2264–2284.

[18] J. Lee, A. Pullan, N. Smith, A computational model of microcirculatory network structure and transient coronary microcirculation, in: Engineering in Medicine and Biology Society, 2004. IEMBS'04. 26th Annual International Conference of the IEEE, Vol. 2, 2004, pp. 3808–3811.

[19] J. Bols, J. Degroote, B. Trachet, B. Verhegghe, P. Segers, J. Vierendeels, A computational method to assess the in vivo stresses and unloaded configuration of patient-specific blood vessels, J. Comput. Appl. Math. 246 (2013) 10–17.

[20] H. Ho, K. Mithraratne, P. Hunter, Numerical simulation of blood flow in an anatomically-accurate cerebral venous tree, IEEE Trans. Med. Imaging 32 (1) (2013) 85–91.

[21] P. Kozlovsky, U. Zaretsky, A. J. Jaffa, D. Elad, General tube law for collapsible thin and thick-wall tubes, J. Biomech. 47 (10) (2014) 2378–2384.

[22] M. Heil, A. L. Hazel, Flow in flexible/collapsible tubes, in: Fluid-Structure Interactions in Low-Reynolds-Number Flows, 2016, p. 280.

[23] M. Aletti, J.-F. Gerbeau, D. Lombardi, A simplified fluid-structure model for arterial flow. application to retinal hemodynamics, Comput. Methods in Appl. Mech. Eng. 306 (2016) 7794.

[24] L. Müller, E. Toro, Enhanced global mathematical model for studying cerebral venous blood flow, J. Biomech. 47 (13) (2014) 3361.

[25] C. Contarino, E. Toro, A one-dimensional mathematical model for dynamically contracting collecting lymphatics: first steps towards a model for the human lymphatic network, in: L. Bonaventura, L. Formaggia, E. Miglio, N. Parolini, A. Scotti, C. Vergara (Eds.), Proceedings of SIMAI 2016, p. 684.

[26] G. Krenz, C. Dawson, Flow and pressure distributions in vascular networks consisting of distensible vessels, Am. J. Physiol. Heart Circ. Physiol. 284 (6) (2003) H2192–2203.

[27] D. Boas, S. Jones, A. Devor, T. Huppert, A. Dale, A vascular anatomical network model of the spatio-temporal response to brain activation, Neuroimage 40 (3) (2008) 1116–1129.

[28] T. David, S. Alzaidi, H. Farr, Coupled autoregulation models in the cerebro-vasculature, J. Eng. Math. 64 (4) (2009) 403–415.

[29] B. C. Fry, T. K. Roy, T. W. Secomb, Capillary recruitment in a theoretical model for blood flow regulation in heterogeneous microvessel networks, Physiol. Rep. 1 (3) (2013) e00050.

[30] P. Causin, F. Malgaroli, A mathematical and computational model of blood flow regulation in microvessels: application to the eye retina circulation, J. Mech. Med. Biol. 15 (02) (2015) 1540027.

[31] S. Čanić, C. Hartley, D. Rosenstrauch, J. Tambaca, G. Guidoboni, A. Mikelic, Blood flow in compliant arteries: An effective viscoelastic reduced model, numerics and experimental validation, Ann. Biomed. Eng. 34 (2006) 575–592.

[32] K. Sriram, B. Y. S. Vázquez, A. G. Tsai, P. Cabrales, M. Intaglietta, D. M. Tartakovsky, Autoregulation and mechanotransduction control the arteriolar response to small changes in hematocrit, Am. J. Physiol. Heart. Circ. Physiol. 303 (9) (2012) H1096–H1106.

[33] J. E. Flaherty, J. B. Keller, S. Rubinow, Post buckling behavior of elastic tubes and rings with opposite sides in contact, SIAM J. Appl. Math. 23 (4) (1972) 446–455.

[34] T. Takahashi, T. Nagaoka, H. Panagida, T. Saitoh, A. Kamiya, T. Hein, L. Kuo, A. Yoshida, A mathematical model for the distribution of hemodynamic paramters in the human retinal microvascular network, J. Biorheol. 23 (77–86) (2009) 2999–3013.

[35] C. E. Riva, J. E. Grunwald, S. H. Sinclair, B. Petrig, Blood velocity and volumetric flow rate in human retinal vessels, Invest. Ophthalmol. Vis. Sci. 26 (8) (1985) 1124–1132.

[36] F. White, Viscous fluid flow, McGraw-Hill, 2006.

[37] V. Vullo, Circular Cylinders and Pressure Vessels, Vol. 3, Springer, 2014.

[38] A. Mikelic, G. Guidoboni, S. Canic, Fluid-structure interaction in a pre-stressed tube with thick elastic walls I: the stationary Stokes problem, Netw. Heterog. Media 2 (3) (2007) 397.

[39] A. R. Pries, B. Reglin, T. W. Secomb, Structural adaptation of vascular networks role of the pressure response, Hypertension 38 (6) (2001) 1476–1479.

[40] P. Lanzer, Mastering endovascular techniques: a guide to excellence, Lippincott Williams & Wilkins, 2007.

[41] J. A. Rhodin, Ultrastructure of mammalian venous capillaries, venules, and small collecting veins, J. Ultrastruct. Res. 25 (5) (1968) 452–500.

[42] S. Timoshenko, J. Goodier, Theory of Elasticity (3rd edit.), McGraw-Hill, New York, 1970.

[43] I. Tadjbakhsh, F. Odeh, Equilibrium states of elastic rings, J. Math. Anal. Appl. 18 (1) (1967) 59–74.

[44] K. Chow, C. Mak, A simple model for the two dimensional blood flow in the collapse of veins, J. Math. Biol. 52 (6) (2006) 733–744.

[45] M. Heil, T. Pedley, Large post-buckling deformations of cylindrical shells conveying viscous flow, J. Fluid Struct. 10 (6) (1996) 565.

[46] I. Simonini, A. Pandolfi, Customized finite element modelling of the human cornea, PloS One 10 (6) (2015) e0130426.

[47] F. Brezzi, M. Fortin, Mixed and hybrid finite element methods, Vol. 15, Springer Science & Business Media, 2012.

[48] R. Sacco, L. Carichino, C. de Falco, M. Verri, F. Agostini, T. Gradinger, A multiscale thermo-fluid computational model for a two-phase cooling system, Comput. Methods in Appl. Mech. Eng. 282 (2014) 239–268.

[49] Microcirculation (Second Edition), Academic Press, 2008.

[50] C. D. Murray, The physiological principle of minimum work i. the vascular system and the cost of blood volume, PNAS 12 (3) (1926) 207.

[51] A. Pries, T. Secomb, T. Gessner, M. Sperandio, J. Gross, P. Gaehtgens, Resistance to blood flow in microvessels in vivo, Circ. Res. 75 (5) (1994) 904–915.

[52] O. Baskurt, M. Hardeman, M. Rampling, H. Meiselman, Handbook of hemorheology and hemodynamics, 1st Edition, Biomedical and health research Vol. 69, IOS Press, 2007.

[53] P. Causin, F. Malgaroli, Blood flow repartition in distensible microvascular networks: Implication of interstitial and outflow pressure conditions., J. Coupled Syst. Multiscale Dyn. 4 (1) (2016) 14–24.

[54] M. Pranevicius, O. Pranevicius, Cerebral venous steal: blood flow diversion with increased tissue pressure, Neurosurgery 51 (5) (2002) 1267.

[55] M. J. Fowler, Microvascular and macrovascular complications of diabetes, Clinical diabetes 26 (2) (2008) 77–82.

[56] G. Drzewiecki, S. Field, I. Moubarak, J. K.-J. Li, Vessel growth and collapsible pressure-area relationship, Am. J. Physiol. Heart. Circ. Physiol. 273 (4) (1997) H2030–H2043.

[57] I. G. Gould, A. A. Linninger, Hematocrit distribution and tissue oxygenation in large microcirculatory networks, Microcirculation 22 (1) (2015) 1–18.

[58] K. Erbertseder, J. Reichold, B. Flemisch, P. Jenny, R. Helmig, A coupled discrete/continuum model for describing cancer-therapeutic transport in the lung, PloS One 7 (3) (2012) e31966.

[59] G. Gadda, A. Taibi, F. Sisini, M. Gambaccini, P. Zamboni, M. Ursino, A new hemodynamic model for the study of cerebral venous outflow, Am. J. Physiol. : Heart Circ. Physiol. 308 (3) (2015) H217.

[60] B. E. Carlson, J. C. Arciero, T. W. Secomb, Theoretical model of blood flow autoregulation: roles of myogenic, shear-dependent, and metabolic responses, Am. J. Physiol.: Heart Circ. Physiol. 295 (4) (2008) H1572.

[61] J. Arciero, A. Harris, B. Siesky, A. Amireskandari, V. Gershuny, A. Pickrell, G. Guidoboni, Theoretical analysis of vascular regulatory mechanisms contributing to retinal blood flow autoregulation, Invest. Ophthalmol. Vis. Sci. 54 (8) (2013) 5584–5593.

[62] C. L. de Lancea, T. David, J. Alastruey, R. G. Brown, Recruitment pattern in a complete cerebral arterial circle, J. Biomech. Eng. 137 (11) (2015) 111004.

[63] G. A. Holzapfel, G. Sommer, C. T. Gasser, P. Regitnig, Determination of layer-specific mechanical properties of human coronary arteries with nonatherosclerotic intimal thickening and related constitutive modeling, Am. J. Physiol. Heart. Circ. Physiol. 289 (5) (2005) H2048–H2058.

[64] R. Z. Zhang, A. A. Gashev, D. C. Zawieja, M. J. Davis, Length-tension relationships of small arteries, veins, and lymphatics from the rat mesenteric microcirculation, Am. J. Physiol. Heart. Circ. Physiol. 292 (4) (2007) H1943–H1952.

[65] G. Guidoboni, A. Harris, S. Cassani, J. Arciero, B. Siesky, A. Amireskandari, L. Tobe, P. Egan, I. Januleviciene, J. Park, Intraocular pressure, blood pressure and retinal blood flow autoregulation: a mathematical model to clarify their relationship and clinical relevance, Invest. Ophthalmol. Vis. Sci. (2014) 13.

Authors' Curriculum Vitae

Paola CAUSIN graduated in Aerospace Engineering at Politecnico di Milano, Italy. She obtained her PhD title in Applied Mathematics at Università degli Studi di Milano, Italy, and she spent post-doc periods at INRIA, France, and EPFL, Switzerland. At present, she is Associate Professor at Università degli Studi di Milano, Italy. Her research deal with mathematical modeling and efficient numerical approximation of multi-scale, multi-physics problems stemming from biological and medical applications.

Francesca MALGAROLI graduated in Mathematics at Università degli Studi di Milano, Italy. At present, she is PhD student in Engineering Mathematics at Politecnico di Milano, Italy. Her research work deal with the mathematical modeling and numerical simulations of microcirculatory networks, with particular focus on the eye retina blood vessels.

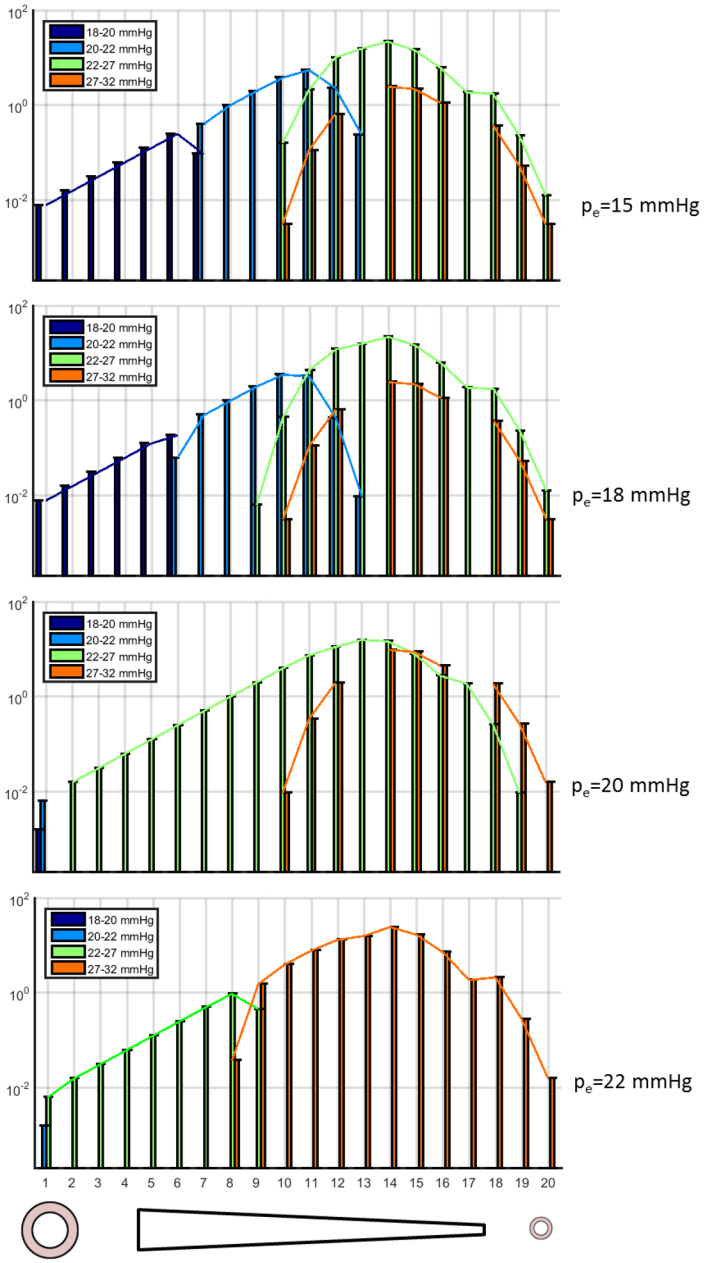

Figure 17: Effect of a local increase of external pressure. The gray shaded region represents the sphere inside which the external pressure is set to $p_e = 20$ mmHg, being elsewhere equal 15 mmHg. Colors code the net variation Δp of blood pressure in the arterial and venous networks. Insets on the right part show zoomed view of the affected network regions.